



Research article



Synergistically engineered magnetic biochar-supported $(\text{BiO})_2\text{CO}_3/\text{Co}_2\text{P-BN}$ ternary photocatalyst for solar-assisted degradation of tetracycline and real effluent treatment

Pooja Dhiman ^a, Manisha Dhiman ^a, Arush Sharma ^b, Manickam Selvaraj ^{c,d}, Mohammed A. Assiri ^{c,d}, Ajay Kumar ^{a,*}

^a Department of Chemistry, School of Basic and Applied Sciences, Maharaja Agrasen University, Solan, 174103, HP, India

^b School of Sciences, Baddi University of Emerging Sciences and Technology, (BUEST) Solan, 173205, Himachal Pradesh, India

^c Department of Chemistry, Faculty of Science, King Khalid University, Abha, 61413, Saudi Arabia

^d Research Centre for Advanced Materials Science (RCAMS), King Khalid University, AlQura'a, P.O. Box 960, Abha, Saudi Arabia

ARTICLE INFO

Keywords:
Photocatalysis
Hetrojunction
Band structure
Tetracycline
Real effluent
Waste water treatment

ABSTRACT

In this study, we introduce a novel ternary heterojunction composite, $(\text{BiO})_2\text{CO}_3/\text{Co}_2\text{P}/\text{BN}$, supported on magnetic biochar, synthesized via an in-situ hydrothermal method. Water pollution by pharmaceutical contaminants, particularly antibiotics like tetracycline (TCN), poses a serious threat to environmental and public health. Conventional treatment methods often fall short in completely removing such persistent pollutants. Hence, the development of efficient, stable, and visible-light-active photocatalysts remains a critical scientific challenge. The innovative design of this composite offers new insights into the enhancement of photocatalytic performance for wastewater treatment. The systematic optimization of synthesis parameters demonstrated a visible-light-active band gap of 2.45 eV and superior light-harvesting capability. The composite material exhibited exceptional catalytic performance in the degradation of tetracycline (TCN) and real effluent samples (RES) collected from the pharmaceutical industry, achieving degradation efficiencies of 96.2 % for TCN and 89.3 % for RES within 1 h under optimized conditions. Notably, the composite also demonstrated remarkable adsorption properties, 92.2 % and 78.4 % adsorption for TCN and RES, respectively, within 2 h. The attained outcomes were accredited to the synergistic interactions among boron nitride, cobalt phosphide and bismuth-oxy-carbonate, which contribute to enhanced charge separation, effective generation of reactive oxygen species (ROS) and a favourable band structure for photocatalysis. Investigations on the influence of operational parameters such as pH, catalyst dosage, and competing ions on catalytic performance were done and hydroxyl radicals were identified as the primary reactive species driving the degradation process. The identification of active pharmaceutical ingredients in RES and mineralization of TCN was established by LC-HRMS, leading to successful elucidation of the degradation mechanism. The high mineralization efficiency was further supported by COD and TOC measurements, reinforcing the potential of this composite for real-world applications. The study, thus, offers a strategic approach to designing next-generation photocatalysts for sustainable environmental cleanup. Finally, the catalyst's reusability over four cycles for RES fortifies its practicality and long-term stability, demonstrating its promise as an effective, environmentally relevant photocatalyst for wastewater treatment.

1. Introduction

The presence of pharmaceutical residues in aquatic ecosystems has been a major concern for the scientific community in recent decades. Complex organic compounds, such as pharmaceuticals, their metabolites, and potential transformation products, are not effectively removed

by conventional wastewater treatment techniques and the inefficient designs of existing treatment plants (Priya et al., 2022). Therefore, these chemical compounds reach all the components of the environment they pose potential adverse effects on prevailing organisms (Khan et al., 2023). Majorities of antibiotics are mostly hydrophilic and were designed to be biologically resistant; they are therefore expected to

* Corresponding author.

E-mail address: ajaydogra972@gmail.com (A. Kumar).

mainly remain in the aqueous phase of the wastewater (de Ilurdoz et al., 2022). Globally, the Tetracycline hydrochloride is one of the most widely produced and consumed antibiotic (Zhang et al., 2024). The majority (~75 %) of tetracyclines consumed by humans and livestock are excreted in an inactive form through urine and feces. This results in elevated concentrations of tetracycline in surface and groundwater, either through runoff or leaching (Wang et al., 2022). As a result, these can lead to antimicrobial resistance, changes in microbial ecology, altered immune responses to pathogens and vaccines, increased susceptibility to infections later in life, and many other effects that are still under investigation (Cocker et al., 2024).

Considering that ineffectiveness of the conventional waste water treatment processes in the removal of residual organic compounds, like pharmaceuticals and their corresponding compounds, alternative more advanced techniques of water treatment are required. Keeping the convenience, easy operability and cost effectiveness in to consideration, adsorption is one of the efficient techniques for the adsorptive removal of the target pollutants from the matrix in the realistic situations. The biomass derived products called as activated carbon, hydrochar and biochar, derived from the pyrolysis of commonly available biomass are proven to efficient in various adsorptive removal processes (Othmani et al., 2021; Ighalo et al., 2022; Aktas et al., 2024). Recently, activated carbon catalysts have been effectively employed in wet oxidation processes using trickle bed reactors, achieving up to 97 % phenol degradation under optimized conditions (Abid et al., 2016). These systems underscore the potential of biomass-derived materials for efficient pollutant removal. Additionally, advanced oxidation processes (AOPs) are also considered alternative to conventional wastewater treatment processes owing to their high efficiency. AOPs are based on the formation of very reactive species that are unselective and enough potential to degrade complex organic compounds. Photocatalysis is one of the AOP that involves a system composed of a photoactive material that absorbs light energy. This energy initiates the generation of various reactive oxygen species (ROS), such as superoxide radicals (O_2^\bullet), hydroxyl radicals ($\bullet OH$), peroxyradicals ($\bullet OOH$), and others, by reacting with dissolved oxygen in the aqueous phase through a series of photochemical chain reactions (Dong et al., 2022; Ahmed et al., 2022; Bi et al., 2024). The transformation of ROS is directly related to the band edge positions of the photocatalysts and their ability to harness energy from incident radiation. In this context, band gap and heterojunction engineering plays a crucial role. However, certain limitations restrict the large-scale application of photocatalysis, including charge recombination, agglomeration, surface area etc when dealing at nano scale. To overcome these limitations, various strategies are currently being employed, including the fabrication of composite-based heterojunctions, the use of appropriate support materials, and doping etc.

Morefurther, among the numerous semiconductor catalysts, cobalt phosphide (Co_2P) is the most commonly utilized in the field of photocatalysis owing to its exceptional physicochemical features and easily tunable bad gap of 1.81 eV (Liang et al., 2021). However, the charge recombination rate restricts the utilization of Co_2P as a sole photocatalyst. Previously published literature has demonstrated that $(BiO)_2CO_3$ (BOC) based composites have significantly contributed to the photodegradation of pharmaceutical contaminants, underscoring the importance of BOC (Zhao et al., 2019). The BOC possesses high oxidation potential owing to its position of valence band edge which lies ≈ 3 eV (Jia et al., 2019; Luo et al., 2023). Recently, various researchers have designed BOC and Co_2P based heterojunctions for diverse photocatalytic applications. For example, Ju et al. synthesized a $BiOBr/Bi_2O_2CO_3$ heterojunction with enhanced charge separation ability, which was effectively utilized for TCN degradation (Ju et al., 2024). Similarly, Sun et al. developed an S-scheme heterojunction composed of $Bi_2O_2CO_3$ anchored with TiO_2 quantum dots for efficient TCN degradation (Sun et al., 2024). Han et al. reported the synthesis of a $TiO_2/CdS/Co_2P$ ternary composite exhibiting multi-step charge transfer capabilities for photocatalytic hydrogen evolution (Han et al., 2025). Likewise, Wu

et al. engineered a Ni-doped Co_2P catalyst with visible-light activity for CO_2 reduction (Wu et al., 2025).

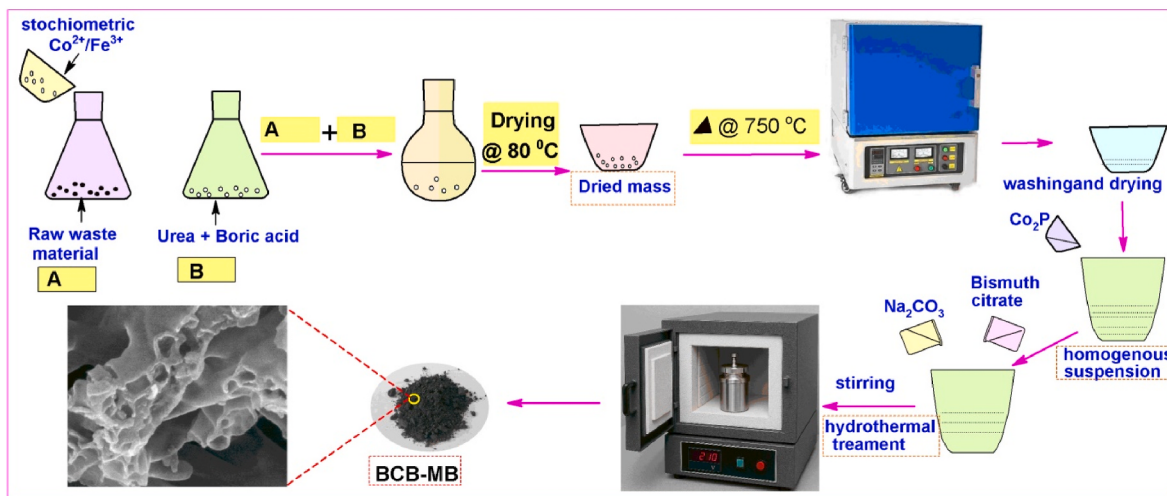
Boron nitride (BN) is an emerging candidate that has recently gained significant interest among researchers for the fabrication of composite-based heterojunctions in the field of photocatalysis. However, the sole use of BN is seldom beneficial in photocatalytic processes due to its wide band gap energy of 5–6 eV, which classifies it as an insulator. However, although various hybrid composites have been synthesized to reduce the band gap, the achieved reductions have often been inadequate. In many cases, the resulting composites exhibit band gaps that remain within the UV region or only slightly extend into the visible spectrum, which significantly limits their feasibility for large-scale practical applications. For instance, Cai et al. reported the synthesis of an $N-ZnO/p-BN$ composite with a band gap of 3.19 eV, which enabled synergistic pollutant removal from water (Cai et al., 2024). Similarly, Chen et al. developed a series of MoS_2/BN nanohybrids, among which the $MoS_2/BN-10\%$ composite showed the most effective degradation performance for Rhodamine B (RhB) and tetracycline (TCN), also possessing a band gap of 3.19 eV (Chen et al., 2024). Similarly numerous composite photocatalysts incorporating boron nitride (BN) have been reported in the literature, in various photo-assisted environmental remediation applications (Recepoglu et al., 2022).

The conversion of waste biomass into valuable materials is considered environmentally benign. Examples of these materials include biochar, activated carbon, and hydrochar. Among them, biochar, which is produced through the pyrolysis of biomass in an oxygen-limited environment and contains approximately 80 % carbonaceous content, is extensively utilized as a support material due to its porous structure and high surface area (Ivanova et al., 2020; Sutar et al., 2022). In addition, the presence of hydroxyl, epoxy, carbonyl, and carboxyl functional groups enhances its potential for use in adsorption processes. As a result, biochar offers a dual advantage: it serves as both, an anchoring substrate for nanomaterials and an effective candidate for pollutant adsorption. Various recent works has proven the efficacy of biochar in photocatalysis and adsorption led waste water remediation techniques (Sutar et al., 2022; Ben Mbarek et al., 2022).

Considering the advantages and disadvantages of each component, a ternary heterojunction comprising BOC, BN, and Co_2P supported on magnetic biochar (BBC-MB) was developed. In this system, biochar functions both as a support material and as an adsorbent for the target pollutant. BN acts as an anchoring material within the heterojunction, while the incorporation of Co_2P and BOC effectively reduces the overall band gap energy of the composite. The successful formation of the heterostructure offers an additional benefit: the presence of a high oxidation potential, as the valence band edges of BN and BOC are positioned above 3 eV. Moreover, the composite demonstrates a lower charge recombination rate. Additionally, the incorporation of magnetic biochar significantly reduces raw material costs while also contributing to the environmental sustainability of the composite. Magnetic separation further minimizes post-treatment expenses, offering operational convenience. Moreover, the use of cost-effective precursors for BN synthesis contributes to the economic feasibility of the composite for large-scale industrial applications. The synthesis of BCB-MB involved optimizing the weight percentage content of each component to maximize its efficiency in Tetracycline removal and remediation of real effluent waster sample based on surface area and optical response.

2. Materials and methods

Bismuth nitrate pentahydrate ($BiNO_3 \cdot 5H_2O$), cobalt nitrate hexa hydrate $Co(NO_3)_2 \cdot 6H_2O$, ferric nitrate neo hydrate $Fe(NO_3)_2 \cdot 9H_2O$, ethanol (C_2H_5OH), boric acid (H_3BO_3), urea (NH_2CONH_2), cobalt chloride hexahydrate ($CoCl_2 \cdot 6H_2O$), sodium hypophosphite (NaH_2PO_2), CTAB, Sodium carbonate (Na_2CO_3) were obtained from Central Drug House (Analytical Reagent grade) and used without further purification. All the reagents were commercially available and used without further



Scheme 1. Brief synthesis methodology opted for BCB-MB fabrication.

purification.

2.1. Collection of raw material for biochar synthesis

The raw materials for biochar production, consisting of mixed biomass, were collected from a garbage site located near the industrial area of Baddi, Himachal Pradesh, India. The biomass primarily included vegetable and fruit peels. The collected biomass was thoroughly washed with distilled water, dried, and then chopped into a fine powder for biochar synthesis using the pyrolysis method.

2.2. Collection of real effluent sample from pharmaceutical industry

The real effluent sample (RES) was collected from a pharmaceutical industry primarily involved in the manufacturing of various drug tablets, located in the Baddi-Barotiwala-Nalagarh (BBN) region of Himachal Pradesh, India, which is widely recognized as one of the largest pharmaceutical hubs in Asia. The obtained effluent sample was centrifuged and filtered to remove any solid substances, and then stored under standard laboratory protocol for further analysis. The sample were tested for pH, Chemical Oxygen Demand (COD), and Biological oxygen demand (BOD) measurements etc. Additionally, High-Resolution Mass Spectrometry (HR-MS) analysis was conducted to detect any residual Active Pharmaceutical Ingredients (APIs) in the RES.

2.3. Methods

2.3.1. Synthesis of magnetic biochar

10-g raw material was first chopped and grinded, followed by washing and drying at 80 °C. $\text{Co}(\text{NO}_3)_2 \cdot 6\text{H}_2\text{O}$ and $\text{Fe}(\text{NO}_3)_2 \cdot 9\text{H}_2\text{O}$ were added in stoichiometric amounts in the crushed raw material. The solid reaction mixture was then transferred to silica crucible followed by heat treatment at 250 °C for two and half hours in the muffle furnace with the heating rate of 10 °C/min under inert atmosphere. After the completion of heat treatment the contents were allowed to cool down to room temperature, thoroughly washed with water/ethanol mixture and finally dried at 80 °C until fully dried.

2.3.2. Synthesis of sole BN

Sole BN was synthesized by the heating the stoichiometric amount of boric acid and urea (1: 24) in a silica crucible in the complete absence of oxygen at 900 °C for 4 h. The resultant white coloured solid mass was washed repeatedly with distilled water and dried in the hot air oven for around 8 h at 80 °C and then labelled as BN.

2.3.3. Synthesis of sole Co_2P

1 mmol of $\text{CoCl}_2 \cdot 6\text{H}_2\text{O}$ was mixed with 5 mmol of NaH_2PO_2 and ground homogeneously in a mortar. The mixture was placed in silica crucible and covered with lid. The corundum boat was heated to 100 °C for 30 min and then heated to 250 °C for 80 min. The whole procedure was carried out under the protection of N_2 gas. The synthesized black product was washed numerous times with distilled water and ethanol, which later dried in the oven for around 8 h at 80 °C, labelled as black Co_2P .

2.3.4. Synthesis of $\text{Bi}_2\text{O}_2\text{CO}_3$

In the typical procedure, 10 mmol of $\text{Bi}(\text{NO}_3)_3 \cdot 5\text{H}_2\text{O}$ was dissolved in 1 mol/L of 10 mL HNO_3 . This transparent solution was labelled as "solution A". 1.0 g CTAB (or 0.4g L-Lysine) and 80 mmol Na_2CO_3 were added to 90 mL distilled water. This transparent solution was labelled as "Solution B". When solution A was added drop-wise in the solution B with continuous stirring, the formation of white coloured milky white suspension. After stirring for 10 min, the mixture was subjected to filtration and repetitive washing with distilled water and ethanol. The obtained white solid product was dried overnight in an oven at 80 °C.

2.3.5. Synthesis of ternary composite $\text{BN}/\text{Co}_2\text{P}/\text{Bi}_2\text{O}_2\text{CO}_3/\text{magnetic biochar (BCB-MB)}$

Initially certain amount of mixed raw waste material, along with stoichiometric amounts of $\text{Co}(\text{NO}_3)_2 \cdot 6\text{H}_2\text{O}$ and $\text{Fe}(\text{NO}_3)_2 \cdot 9\text{H}_2\text{O}$, ($\text{Co}^{2+}/\text{Fe}^{3+}$, molar ratio 1:2) were suspended in 100 mL of absolute ethanol and mechanically stirred (Remi RQ) to obtain a slurry (Mixture A). In a separate vessel, a solution containing boric acid and urea in a 1:24 (w/w) ratio was prepared (Mixture B). Mixtures A and B were combined and mechanically stirred for 10 min to achieve a uniform slurry. The resulting mixture was then dried at 80 °C in a vacuum oven (Remi RVO-50) to obtain a dry mass. This mass was further annealed in a muffle furnace (Harrier, HE-MF-1200p, 1150 ± 1 °C) at 750 °C with a heating rate of 10 °C/min under an inert atmosphere of N_2 . The contents were allowed to cool, and the obtained mass was washed several times with a water and ethanol mixture to remove any unreacted substances. Finally, the product was dried and stored for further use.

In the second step, a certain amount of the obtained mass was suspended in 80 mL of distilled water along with a specified amount of pre-synthesized Co_2P . The suspension underwent ultrasonication (Phoenix, 40 KHz) for 10 min. To this suspension, 6.4 g of bismuth citrate and 1.84 g of Na_2CO_3 were added, followed by mechanical stirring for 20 min. The reaction mixture was then transferred to a Teflon-lined hydrothermal autoclave and thermally treated in muffle furnace at 180 °C for 12 h. After the reaction was complete, the product was washed and dried in a

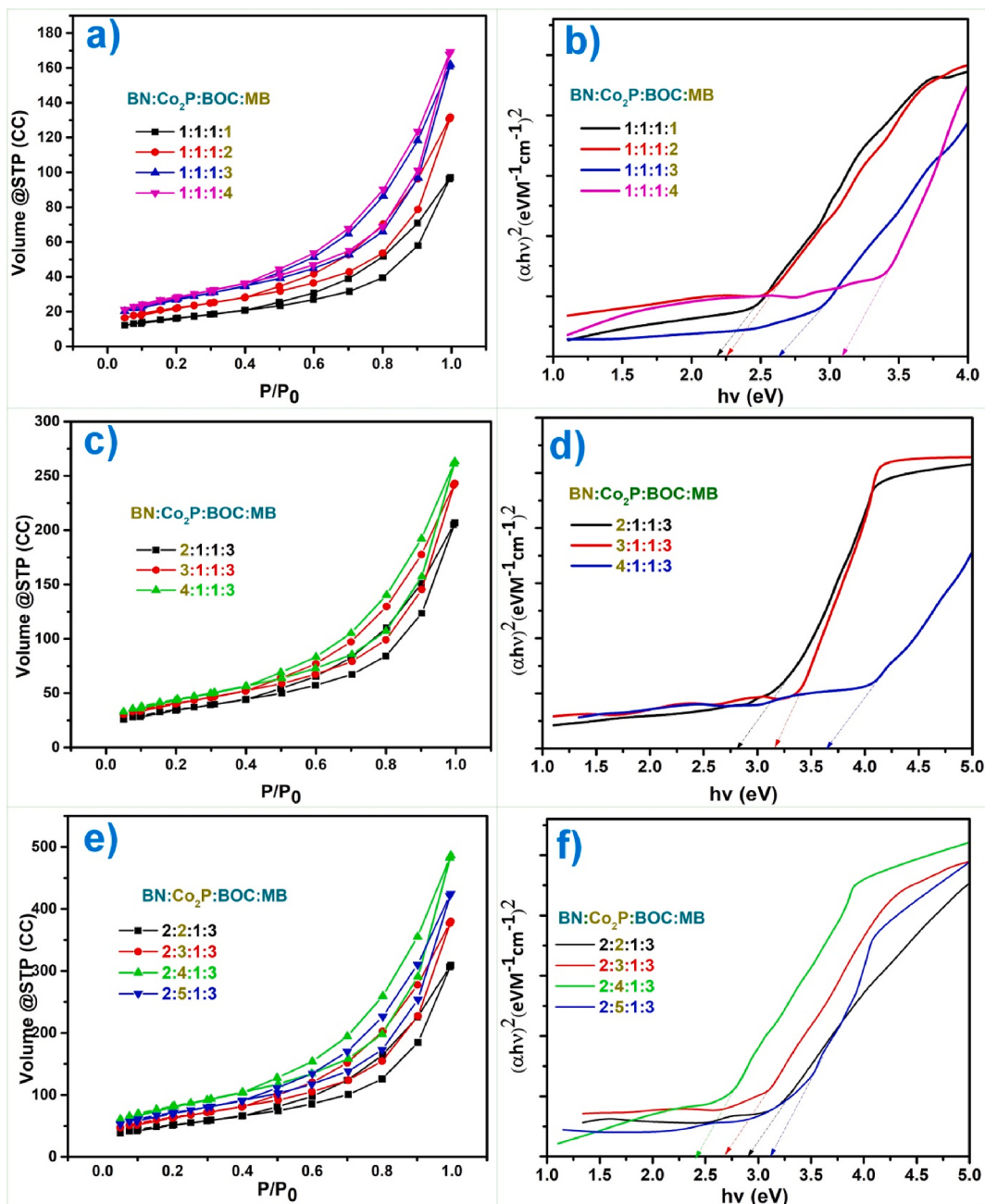


Fig. 1. Content optimization of BCB-MB at different wt% ratios with corresponding analyses: (a), (c), (e) BET surface area; (b), (d), (f) band gap measurements.

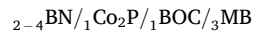
vacuum oven at 80 °C. The entire synthesis procedure was summarized in **Scheme 1**. The methodology for the synthesis of binary composite with and without magnetic biochar has been shown in text S1.

2.3.6. Content optimization in BCB-MB with the BN, Co₂P and MB

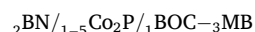
$_{2-4}\text{BN}/_{1-5}\text{Co}_2\text{P}/_{1-3}\text{BOC}/_{1-4}\text{MB}$ (here the numerical subscript at the lower left corner represents constant wt% while the numerical-range subscript represent the range selected for optimization)

The rationale behind the optimization of counterpart content is to investigate how the individual entity affects the properties of the BCB-MB composite such as surface area, band gap and potential toward the adsorption of TCL. In the first step the ratio (w/w) of BN, Co₂P and BOC kept constant while the ratio of MB was varied from 1 wt% to 4 w%. This analysis shows that the BET surface area increases from 90 to 170 m²/g respectively (Fig. 1(a)). But if we see the band gap values, we can see a blue shift in band gap from 2.2 to 3.2 eV. As 3.2 eV touches the edge of

wide band gap factor as depicted in Fig. 1 (b). So from here we have chosen 3 wt% of magnetic biochar content for the next step.



In this step, the BN content was varied from 2 wt% to 4 wt%. As observed, the surface area increased with the rise in BN content, as illustrated in Fig. 1(c). However, at 3 wt% BN content, followed by 4 wt% a blue shift in the band gap was noticed, reaching approximately 3.6 eV Fig. 1 (d). Therefore, 2 wt% BN was selected as the optimal concentration for further studies. Although the 3 & 4 wt% BN content exhibited a higher surface area, but its ability to harness light under visible conditions may be limited.



In this step, the Co₂P content variation was studied in the range of 1–5

wt%. The analysis showed that as the Co₂P content increased from 2 wt % to 4 wt%, the BET surface area (Fig. 1 e) also increased, accompanied by a reduction in band gap values (Fig. 1 f). This trend can be attributed to the fact that Co₂P acts as a narrow band gap photocatalyst. However, anomalies were observed at 5 wt%, where a decrease in BET surface area and a blue shift in the band gap were noted. This anomalous behaviour can be attributed to the fact that when the Co₂P concentration exceeds a certain threshold, it may act as a separate entity distinct from the heterojunction. Consequently, this can lead to agglomeration, which potentially obstructs the path of solar illumination.

Based on the above content optimization, we have selected BCB-MB with a content ratio (w/w%) of 2BN/4Co₂P/1BOC/3MB, as it demonstrated the best performance in terms of surface area and visible light-active band gap. This ratio was normalized to 0.5BN/1Co₂P/0.25BOC/0.75MB. The overall synthesis optimization information for individual content was listed in Table S1.

2.3.7. Experimental setup for adsorption removal of TCN and RES

Initially, a specific amount of BCB-MB was suspended in a solution containing TCN, and the resulting pollutant-adsorbent suspension was incubated in a thermal shaker at 100 RPM for a predetermined period. Subsequently, the residual concentration of TCN in the solution was estimated by withdrawing aliquots at regular intervals and analyzing them using double-beam UV-Vis spectroscopy at λ_{max} 383 nm using the following equation:

$$\% \text{ adsorption} = \frac{C_0 - C_t}{C_0} \times 100 \quad (1)$$

where, C_0 is the initial and C_t is final concentration of TCN (mg/L).

Under similar experimental setup the adsorption removal of API residue from RES were studied by the help UV-Vis spectroscopy (Labtronics LT-1900). In case of RES, a scan between 200 and 700 nm was run to obtain λ_{max} . The % adsorption was calculated on the basis of following equation:

$$\% \text{ adsorption} = \frac{A_0 - A_t}{A_0} \times 100 \quad (2)$$

where, A_0 is the initial and A_t is final absorbance of RES.

2.3.8. Experimental setup for photocatalysis of tetracycline (TCN) and real effluent (RES)

The photocatalysis experiment was conducted under simulated visible light irradiation using a 500 W Xe lamp. A 200 mL double-walled quartz vessel equipped with a water circulation system was used for the reaction. Initially, 100 mL of TCN pollutant solution (60 mg L⁻¹) was prepared and mixed with a specified concentration of photocatalyst. The lamp was positioned vertically at a height of 15 cm above the reactor. Afterward, the degradation process was started by switching the lamp on, with occasional gentle stirring. The progress of photocatalysis process was monitored by the double beam UV-Vis spectrophotometer. The degradation and mineralization of TCN and RES was examined by COD and HR-MS analysis.

2.4. Characterization

The FTIR spectrum of photo-catalyst was conducted in the transmission mode between 4000 and 400 cm⁻¹ using a PerkinElmer - Spectrum RX-IIFTIR. X-ray diffraction analysis was carried out by using a Panalytical's X'Pert Pro (Cu-K α radiation, Ni as β filter. The specific surface area was measured using N₂ sorption by a NOVA 1200 analyser and calculated using Brunauer–Emmett–Teller (BET) method (degassing time 5 H, under vacuum at 150 °C). X-ray photoelectron spectroscopy (XPS) analysis was conducted deploying thermo Scientific NEXSA with monochromatized Al K- α radiation (1489.6 eV). The ultraviolet-visible spectra (UV-vis) were recorded using a Shimadzu 2202 double beam

spectrophotometer. Photoluminescence (PL) spectroscopy was performed using a PerkinElmer LS6500 fluorescence spectrophotometer. Surface morphology and elemental analysis has done by scanning electron microscopy by utilizing Nova Nano SEM 450. Transmission electron microscopy (TEM) imaging was done using a Tecnai G 2 20 S-TWIN instrument.

2.5. Photoelectrochemical analysis

Flat band potential analysis was systematically carried out using a Sherwood Scientific MK1 MSB workstation (220 V, 50 Hz) in a standard three-electrode configuration. In this setup, a platinum wire served as the counter electrode, an Ag/AgCl electrode (saturated KCl) was used as the reference, and the catalyst-coated FTO substrate acted as the working electrode. The measured potentials versus Ag/AgCl were converted to the normal hydrogen electrode (NHE) scale using the equation:

$$E_{\text{NHE}} = E_{\text{Ag/AgCl}} + 0.205 \text{ V} \quad (3)$$

Here, $E_{\text{Ag/AgCl}}$ is the experimentally recorded potential, and 0.205 V accounts for the standard potential offset of the Ag/AgCl reference at 25 °C.

For the preparation of the working electrode, 10 mg of the photocatalyst powder was dispersed in 5 mL of an ethanol/water mixture (4:1 v/v) and ultrasonicated for 5 min to obtain a uniform suspension. To improve film adhesion and stability, 20 μL of Nafion solution was added as a binder. The resulting slurry was drop-cast evenly onto a pre-cleaned fluorine-doped tin oxide (FTO) glass substrate ($1.5 \times 1.5 \text{ cm}^2$) and left to dry under ambient conditions. Photocurrent and flat band potential measurements were conducted under illumination using a 300 W Xenon lamp equipped with an appropriate cut-off filter to simulate solar light. The system was purged with nitrogen prior to measurements to eliminate oxygen interference.

2.6. Band gap and spectral analysis

The analysis was carried out to investigate spectral response and band gap energy. For this 20 mg of the catalysts was suspended in 20 mL of anhydrous ethanol followed by the sonication for 10 min to obtain a uniform suspension. The optical response of the suspension was recorded in a double beam UV-Vis spectrophotometer in the range 200–800 nm.

(Kumari et al., 2025). The band gap analyses were computed using the following equation:

$$\alpha h\nu = B(\hbar\nu - E_g)^n \quad (4)$$

where α absorption coefficient (2.303 A/L), E_g represents the band gap, B is the band tailing parameter, $h\nu$ denotes the photon energy. The parameter n is determined by the type of optical transition (either direct or indirect). The band gap was determined by extrapolating the linear portion of the $(\alpha h\nu)^2$ vs $h\nu$ curve to the point where α equals zero.

The conduction and valence band edges were determined by the equation:

$$E_{\text{VB}} = \chi \cdot E_e + 0.5E_g \quad (5)$$

$$E_{\text{CB}} = E_{\text{VB}} - E_g \quad (6)$$

where, EVB and ECB are the edges of valence and conduction band respectively, E_e is the energy of the free electrons on hydrogen scale (~4.5 eV), χ is the geometric mean of the absolute electronegativity on Pearson scale (PAE) and E_g is the band gap energy of photocatalyst in eV. The photoluminescence analysis was also carried out for the synthesized materials to see the fate of charge recombination rate.

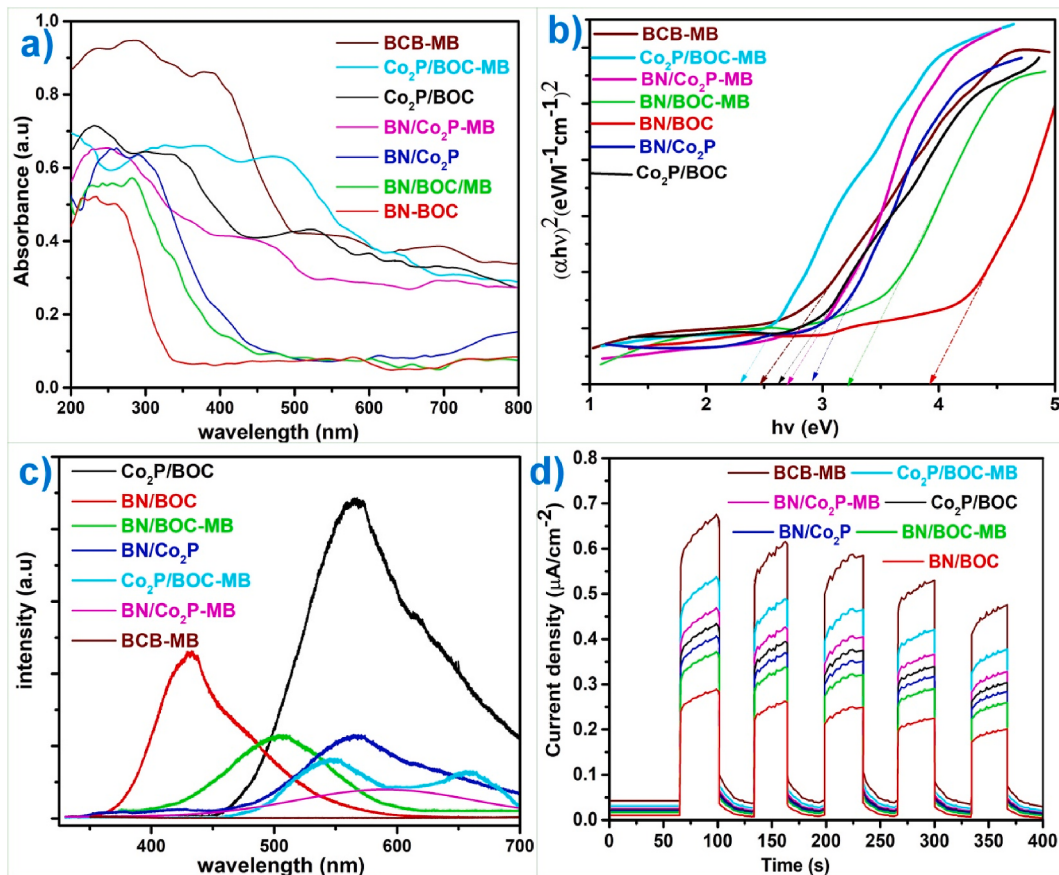


Fig. 2. (a) UV-Vis DRS spectra, (b) Tauc plots, (c) PL analysis and (d) Photo-current response analysis for BCB-MB and their counterparts.

3. Result and discussion

3.1. Optical properties and spectral response

A detailed analysis of the optical and spectral response of BCB-MB was conducted. The optical responses of the individual binary

counterparts with and without the magnetic biochar component, based on the optimized wt % ratio in BCB-MB were evaluated and compared to gain insights into the behavior of each component and their contribution to the overall spectral performance. Tables S2 and S3 provides details of the binary composites with and without magnetic biochar used in the optimized BCB-MB formulation selected for optical analysis. Fig. 2 (a)

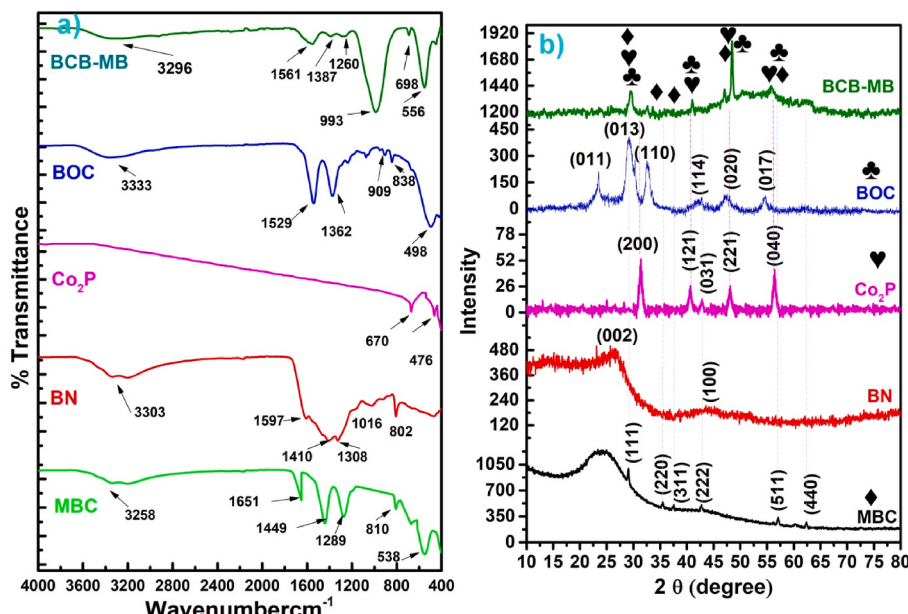


Fig. 3. (a) FT-IR spectra and (b) XRD spectra of BCB-MB & its counterparts.

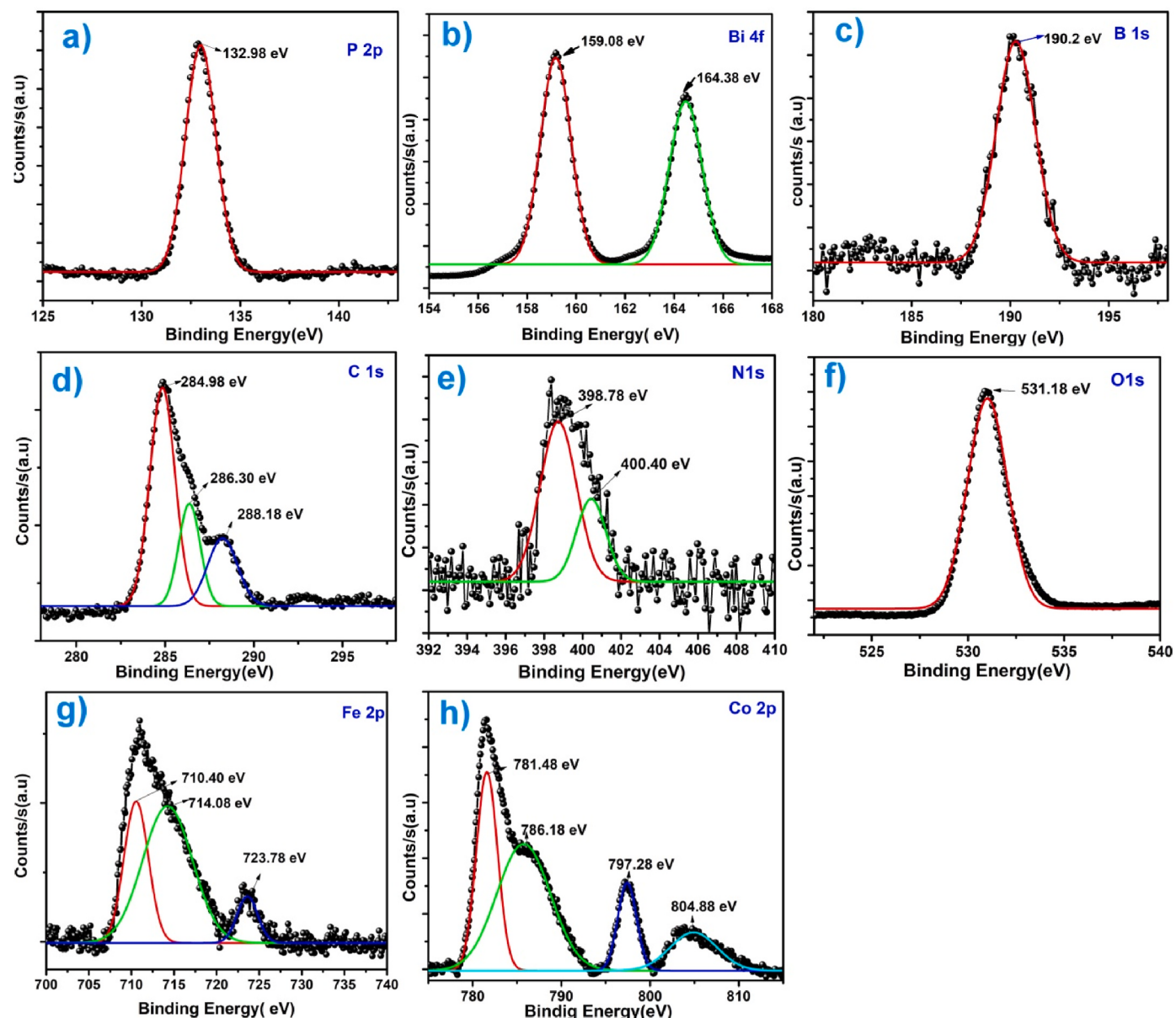


Fig. 4. Deconvoluted XPS spectra of BCB-MB (a) P 2p (b) Bi 4f (c) B 1s (d) C 1s (e) N 1s (f) O 1s (g) Fe 2p and (h) Co 2p.

illustrates the light absorption behaviour of the synthesized catalysts under UV-Vis irradiation, while the corresponding Tauc plots derived from the absorption spectra are presented in Fig. 2(b).

The results show that BCB-MB exhibits higher potential for light absorption compared to other catalysts. This enhanced performance is attributed to the synergistic effect, which integrates the individual light-responsive properties of the components into a single fabricated photocatalyst (BCB-MB), leading to improved optical absorption and photocatalytic efficiency. The band gap (E_g) values computed from Tauc plots were 2.45, 2.32, 2.71, 3.24, 2.63, 2.91, and 3.94 eV for BCB-MB, Co₂P/BOC-MB, BN/Co₂P-MB, BN/BOC-MB, Co₂P/BOC, BN/Co₂P, and BN/BOC, respectively. The results indicate that catalysts containing Co₂P exhibit a narrower band gap compared to those with BN and BOC in their composition. This suggests that Co₂P plays a crucial role in reducing the band gap energy, enabling the catalysts to efficiently absorb visible light. Meanwhile, BN and BOC contribute primarily to the reduction of charge recombination rates, enhancing overall photocatalytic performance. In the overall BCB-MB composite the magnetic biochar serves to provide a porous surface with various anchoring sites,

which help to minimize the agglomeration.

The PL analysis presented in Fig. 2(c) and details such as excitation wavelength was supplied under Table S4. The analysis shows that, except for BCB-MB, the other catalysts exhibit emission peaks due to the fast charge recombination rate. In contrast, for BCB-MB, the emission peak nearly disappears and becomes flattened compared to the other catalysts. This suggests that BCB-MB facilitates heterojunction formation and reduces the lifetime of photoinduced charge carriers. Furthermore, Fig. 2(d) represents the photocurrent response analysis of BCB-MB and its counterparts. The analysis indicates that BCB-MB exhibits high charge mobility due to heterojunction formation, which enhances the transport of photoinduced free electrons and contributes to improved surface activity toward photocatalytic processes. These results are consistent with the findings from the PL analysis.

3.2. FTIR analysis

The FTIR spectra of magnetic biochar, BN, Co₂P, BOC and BCB-MB have been given in Fig. 3(a). For magnetic biochar the peak around

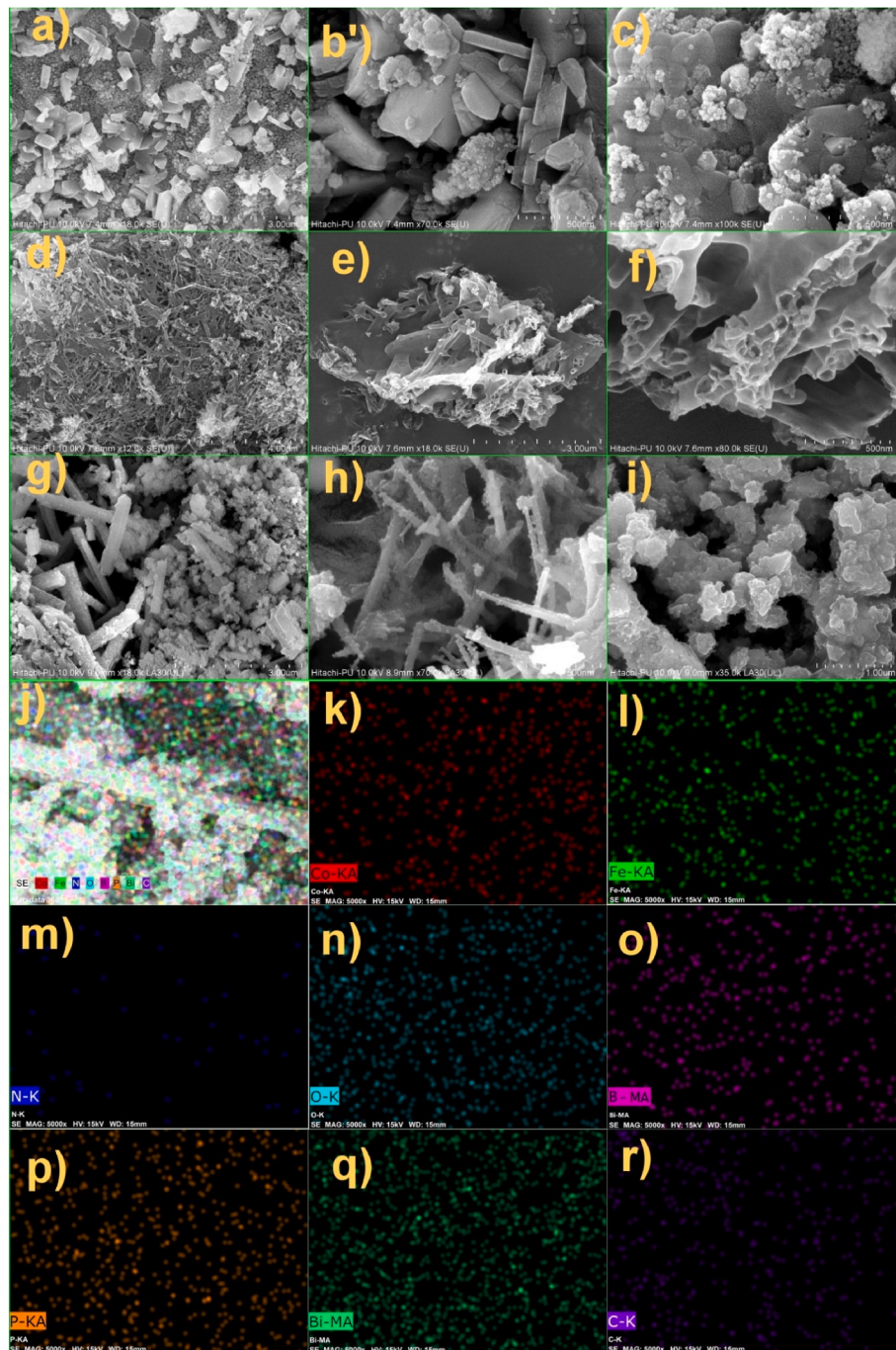


Fig. 5. SEM micrographs: (a–c) magnetic biochar, (d–f) BN, (g–i) BCB-MB & (j–r) elemental mapping of BCB-MB.

1651 cm⁻¹ is attributed to the stretching vibrations of aromatic >C=C< or >C=O, indicating the presence of surface functional groups (Ilić et al., 2022). The peaks observed at 1449 cm⁻¹ and 1289 cm⁻¹ are ascribed to C–H bending and C–O stretching vibrations, respectively. The peak at 810 cm⁻¹ is commonly associated with out-of-plane bending vibrations of C–H bonds, while the peak around 530 cm⁻¹ may be attributed to the vibrational modes of the metal–oxygen bond related to magnetic components (Kumar et al., 2017a, 2017b). For BN, the peak around 1597 cm⁻¹ along with 1308 cm⁻¹ and 1410 cm⁻¹ ascribed to the E_{2g} and E_{1u} mode of in-plane B–N stretching vibration respectively. The peak around 1016 and 802 cm⁻¹ corresponds to B–N bending & B–N–B out of plane bending vibration (Shahabuddin et al., 2018; Choi et al., 2015; Ji et al., 2020). For pure Co₂P, absorption peak at 670 and 470 cm⁻¹ accounts for Co–P stretching or bending vibration (Yazdi et al., 2022). FTIR spectrum

of pure Bi₂O₂CO₃ (BOC) The broad band around 3283 cm⁻¹ can be assigned to –OH stretching vibration while the peak at 1529 cm⁻¹ may be assigned for bending vibration of –OH. More further, the band at 1362 cm⁻¹ assigned to anti-symmetric v3 vibrations, while peaks at 909 cm⁻¹ and 509 cm⁻¹ are correspond to out of plane bending v1, v2 mode for the CO₃²⁻ ion (Chandel et al., 2022). The FTIR spectrum of BCB-MB reflects several major peaks; however, some slight shifts were observed, most likely due to interactions between the different components, indicating successful integration within the fabricated composite material.

3.3. XRD analysis X-ray diffraction analysis

Fig. 3 (b) shows the XRD patterns of Magnetic biochar (MB), Boron nitride (BN), Co₂P and (BiO)₂CO₃ (BOC). For magnetic biochar the

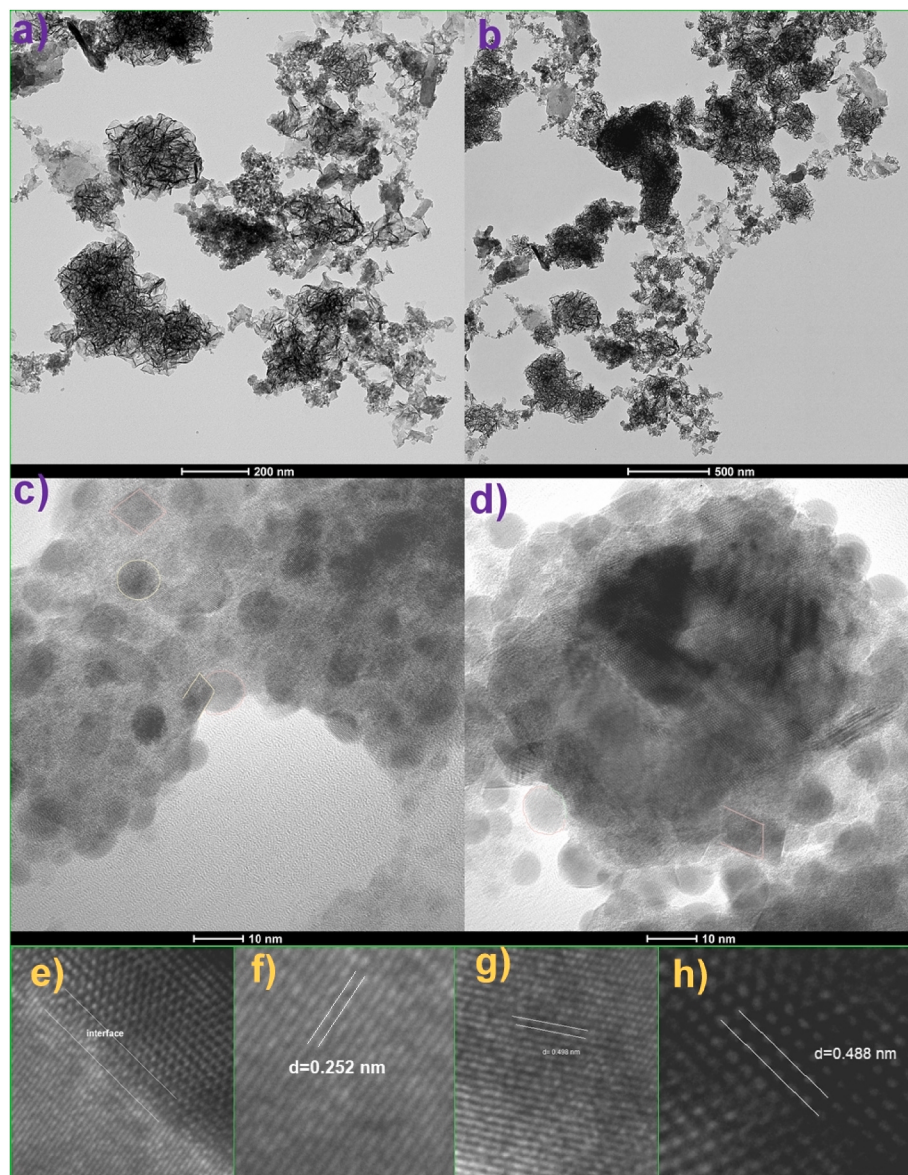


Fig. 6. (a–b) low resolution,(c-e) high resolution TEM images for BCB-MB and (f-h) interlayer d-spacing in BCB-MB for BOC, Co₂P, and BN respectively.

diffraction peaks for the magnetic component (CoFe_2O_4) appeared at 2θ values 29.1° (111), 35.3° (220), 37.3° (311), 42.7° (222), 56.2° (511) and 62.2° (440) indicating the spinal type of magnetic ferrite. The diffraction data was in good agreement with the standard JCPD file no. 00-22-1086 (Huang et al., 2015). Additionally, a broad peak at 24.4° was observed, which is commonly regarded as a signature peak of the turbostratic phase of microcrystalline and amorphous carbon in biochar. For BN, two diffraction peaks were observed at 2θ values of 26.1° (002) and 44.5° (100); for Co₂P the diffraction peaks at 31.4° , 40.6° , 42.8° , 48.1° and 56.3° were appeared which corresponds to planes (220), (121), (031), (221) and (040) respectively. The diffraction peaks for BN and Co₂P were found to matching well with JCPDS 34–0421 & 32–0306 respectively (Jiang et al., 2019; Shankar et al., 2019). Furthermore, for BOC the diffraction peaks appeared at 23.5° , 29.1° , 32.3° , 42.7° , 46.9° , 52.6° which ascribed for (011), (013), (110), (114), (020) and (017) diffraction plane. The diffraction data for BOC is in good agreement with the standred JCPDS No. 41–1488 (Wang et al., 2018a). Furthermore, the XRD pattern of BCB-MB shows the consolidated diffraction peaks to corresponding counterpart. However, some of peaks seem to be merged with another while some of the peaks was not observed which may hints

for the successful fabrication and consolidation of each counterpart in a single composite system (Jaiswal et al., 2024; Kumar Bhoi et al., 2020).

3.4. XPS study

X-ray Photoelectron Spectroscopy (XPS) analysis was conducted to investigate the chemical states and elemental composition of the MB-BCB composite. The survey spectrum, presented in Fig. S1 and Fig. 4, confirms the presence of B, N, Co, P, C, Bi, Fe, and O on the surface of the composite. Fig. 4(a) shows the XPS spectrum of P 2p, which displays a single peak at 135 eV, indicating the presence of phosphorus (Wang et al., 2018b). The deconvoluted spectrum of Bi, shown in Fig. 4(b), reveals two characteristic peaks at 159.09 eV and 164.38 eV, corresponding to Bi 4f_{7/2} and Bi 4f_{5/2}, respectively, which are attributed to the Bi³⁺ oxidation state in $\text{Bi}_2\text{O}_2\text{CO}_3$ (Du et al., 2022). In Fig. 4(c), the B 1s spectrum exhibits a single peak at 190.2 eV, confirming the presence of boron (Feng et al., 2019). Fig. 4(d) shows the C 1s spectrum with two fitted peaks: one at 284.98 eV, corresponding to the carbon species of biochar, and another at 286.30 eV, attributed to carbonate ions (CO_3^{2-}) in $\text{Bi}_2\text{O}_2\text{CO}_3$. A deconvoluted peak at 288.98 eV further supports this

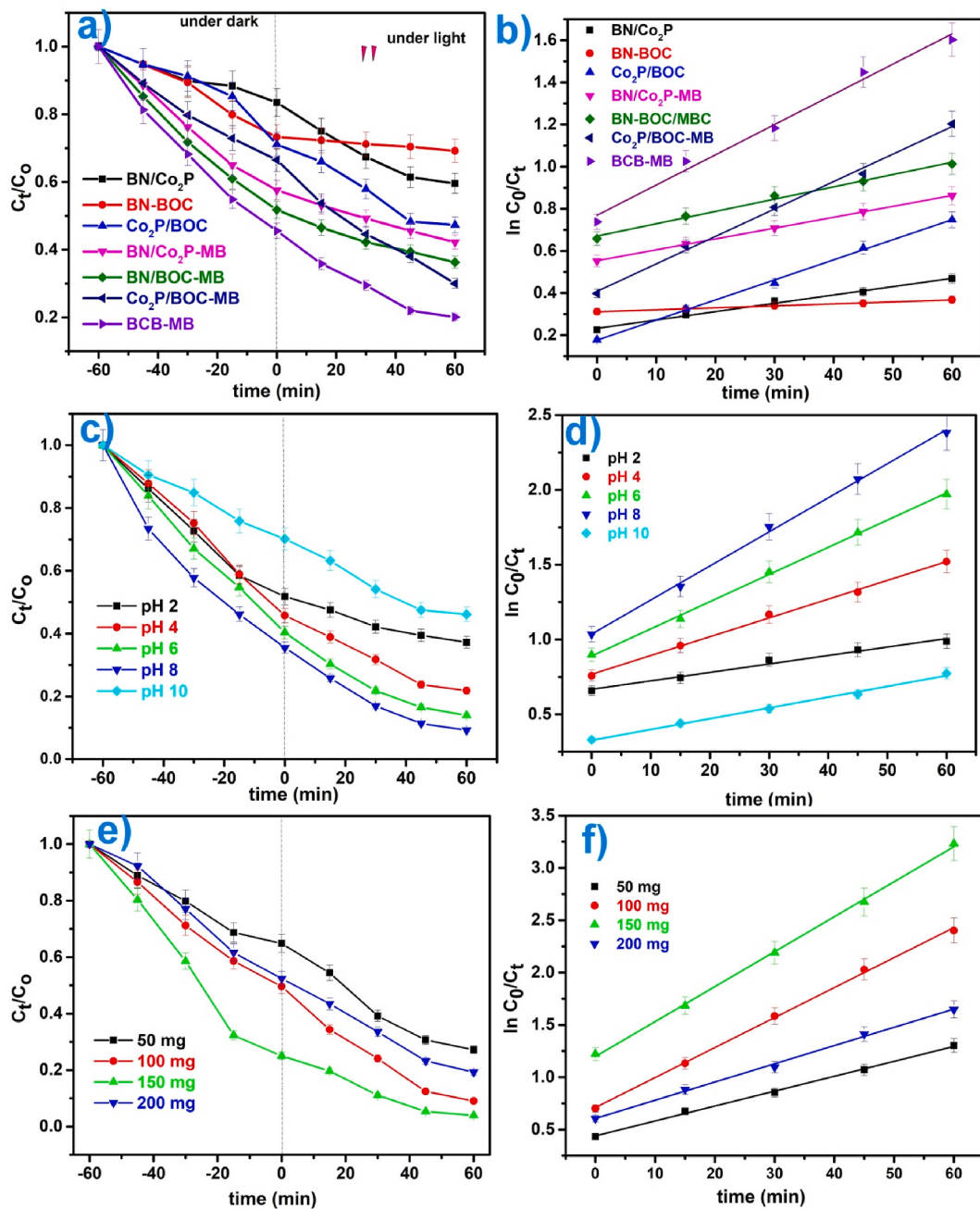


Fig. 7. (C_t/C_0) as a function of time and corresponding pseudo-first order kinetic plots for BCB-MB assisted TCN degradation (a)–(b), effect of pH (c)–(d) and catalyst dosage (e)–(f).

assignment (Chandel et al., 2022; Ayiania et al., 2020). The N 1s spectrum in Fig. 4(e) exhibits two peaks at 398.78 eV and 400.40 eV, indicating the presence of different nitrogen species (Feng et al., 2019). Fig. 4(f) displays the O 1s spectrum with a distinct peak at 531.18 eV, which corresponds to oxygen in Bi₂O₂CO₃ (Kwoka et al., 2022). Fig. 4(g) presents the Fe 2p spectrum, showing two peaks at 710.40 eV and 723.78 eV, corresponding to Fe 2p_{3/2} and Fe 2p_{1/2}, respectively. The Fe 2p_{3/2} peak is further split into components at 714.08 eV, which are attributed to Fe²⁺ and Fe³⁺ species (Li et al., 2020; Hughes et al., 2024). Finally, Fig. 4(h) confirms the presence of Co through the Co 2p spectrum, which displays characteristic peaks at 781.48 eV (Co 2p_{3/2}) and 797.28 eV (Co 2p_{1/2}). The satellite peaks at 786.18 eV and 804.88 eV further confirm the chemical state of cobalt (Zhang et al., 2020; Zhu et al., 2023).

3.5. FE-SEM and TEM analysis

Fig. 5 depicts the surface micrographs of the prepared materials. Fig. 5(a–c) shows the micrographs of the magnetic biochar, which reveals the presence of magnetic CoFe₂O₄ on the rough surface of the biochar with a mixed array of arrangement (Liu et al., 2024). Fig. 5(d–f) present micrographs of BN at different resolutions, revealing a network of hollow rod-like structures. This morphology is highly advantageous for supporting nanoparticles or hetero-junctions, as well as for adsorption processes, due to the abundance of active sites that facilitate entanglement or interaction with other materials (Wang et al., 2018c). Fig. 5(g–i) shows the micrographs of BCB-MB, demonstrating the mixed morphology of its components. The rod-like structures corresponding to BN, while small cube-like structures with rough surfaces are observed, representing the magnetic component and biochar, respectively.

(Susanti et al., 2022). In Fig. 5 (h), the rod-like BN structures appear entangled within the biochar matrix, whereas Fig. 5(i) reveals microfloral structures of BOC, which might be intermixed with Co₂P (Dutta et al., 2021; Veettil Vineesh et al., 2020). Furthermore, the elemental mapping of the composite is presented in Fig. 5(j–r) confirming the B, N, Co, P, C, Bi, Fe, and O elemental composition of BCB-MB.

In Fig. 6 depict the TEM micrographs where Fig. 6 (a & b) depict the microfloral structure of BOC, entangled with rod-shaped BN, is clearly visible along with tiny, particle-like morphologies (Cheng et al., 2010). The darker regions in these micrographs represent areas of high electron density, which may correspond to CoFe₂O₄ and Co₂P counterparts intercalated within the porous biochar matrix (Liang et al., 2021; Li et al., 2024a). High-resolution micrographs are presented in Fig. 6 (c & d), revealing mixed morphologies, including oval, spherical, and rectangular structures. The interface observed in Fig. 6 (d & e) clearly demonstrates the interfacial contact between the BCB-MB components. The interlayer spacing for BOC, Co₂P, and BN was calculated to be 0.252 nm, 0.498 nm, and 0.488 nm, as shown in Fig. 6(f–h) respectively.

3.6. Removal of TCN from simulated wastewater

3.6.1. Adsorption removal of TCN

Fig. S2 illustrates the percentage adsorption profile of TCN by BCB-MB and its counterpart composites under dark conditions over a period of 2 h. The influence of composite composition on adsorption performance is clearly evident from the analysis. The binary composite without MB Co₂P/BOC exhibits an adsorption efficiency of 36.3 %, while BN/Co₂P and BN/BOC shows adsorption values of 43.5 % and 54.2 %, respectively. These findings indicate that the incorporation of BN enhances the adsorption capability of Co₂P-based composites, likely due to BN's high surface area and stronger interaction with pollutant molecules. The introduction of MB significantly improved the adsorption performance across all composite systems. Specifically, Co₂P/BOC-MB achieved an adsorption of 60.3 %, BN/Co₂P-MB 81.4 %, and BN/BOC-MB 86.6 %. Notably, the ternary composite BCB-MB exhibited the highest adsorption efficiency; reaching 92.2 %. This enhanced performance is attributed to the synergistic effects of the individual components. BN contributes a high surface area and excellent chemical stability, while MB enhances porosity, magnetic properties, and active site accessibility. The BCB-MB system uniquely demonstrates synergistic compositional advantages and underscores the significant potential of MB in improving adsorption processes.

3.6.2. Photocatalytic removal of TCN

The experiment was conducted using simulated polluted water containing TCN as the targeted pollutant moiety. Additionally, the efficiency of the prepared catalysts was tested on real polluted water samples (RES), with the results discussed further in the subsequent section. The simulated wastewater sample, containing the desired dosage of photocatalyst, was exposed to a radiation source, and the degradation study was evaluated. Fig. 7 (a) illustrates the reduction of TCN conc. (C_t/C_0) as a function of time. Approximately 79.3 % of TCN was degraded within 1 h of the experiment. The experiment depict that TCN meagrely undergoes self-photolysis. The degradation efficiency of BCB-MB was compared with its optimized counterparts demonstrate its superior performance. The order of compared degradation efficiency in terms of rate constant is recorded as following: BCB-MB ($k_1 = 0.0143$), Co₂P/BOC-MB ($k_1 = 0.0130$), BN/BOC-MB ($k_1 = 0.0098$), BN/CO₂P/MB ($k_1 = 0.0085$), Co₂P/BOC ($k_1 = 0.0075$), BN/Co₂P ($k_1 = 0.0048$), BN/BOC ($k_1 = 0.0039$). The results obtained from the kinetic analysis as shown in Fig. 7 (b) indicate that the degradation process follows a pseudo-first-order model. The superior performance of BCB-MB ($k_1 = 0.0143$) can be attributed to the optimized characteristics of its individual components. The magnetic biochar offers a porous surface enriched with functional groups, which facilitates the adsorption and entrapment of pollutant molecules and provides active sites for the

Table 1

Effect of pH on the photo-degradation rate of TCN by BCB-MB.

pH	02	04	06	8	10
k_1 (min ⁻¹)	0.0056	0.0125	0.0181	0.0227	0.0072

Table 2

Effect of varying catalysts dosage on the degradation rate of TCN.

Dosage (mg L ⁻¹)	50	100	150	200
k_1 (min ⁻¹)	0.0142	0.0286	0.0334	0.0174

integration of hetero-structures, thereby minimizing agglomeration. BN functions as an efficient charge carrier, effectively reducing photoinduced charge recombination. Likewise, Co₂P and BOC contribute to enhance light harvesting. The synergistic integration of these components within the BCB-MB composite leads to the formation of a favourable band structure with a visible-light-active band gap, enabling efficient light absorption and utilization, ultimately enhancing the overall photocatalytic performance of the composite material.

3.6.3. Effect of pH

pH is a critical parameter that significantly influences the photocatalytic process, as it affects the surface charge properties of both the catalyst and the pollutant molecules. In general, the efficiency of a photocatalyst largely depends on its ability to retain pollutant molecules in close proximity, which is governed by attractive interactions such as electrostatic forces and van der Waals interactions. Analyzing the chemical structure of tetracycline (TCN) (Fig. S3), it is evident that the molecule exhibits three distinct pKa values (3.3, 7.3, and 9.4) (Wang et al., 2019). These pKa values suggest that the molecular charge state of TCN varies with pH, thereby influencing its interaction with the catalyst surface. The effect of pH on the degradation of TCN using the BCB-MB photocatalyst was investigated over a pH range of 2–10. The corresponding results are presented in Fig. 7 (c & d), with rate constants provided in the accompanying Table 1. The degradation efficiencies observed at various pH levels were as follows: pH 8 (90.6 %), pH 6 (86.3 %), pH 4 (78.4 %), pH 2 (63.2 %), and pH 10 (53.6 %). These results indicate that near-neutral to slightly alkaline conditions are most favourable for the photocatalytic degradation of TCN using the BCB-MB catalyst.

This observed trend can be explained based on the interaction between the TCN molecule and the catalyst's surface, which depends on the pKa constants of TCN and the zero-point charge (ZPC) of the catalyst. The ZPC of BCB-MB was determined to be approximately 8.3, as shown in Fig. S4. This indicates that when the pH is above the ZPC, the catalyst surface becomes negatively charged, and when the pH is below the ZPC, the surface becomes positively charged. A similar principle applies to the TCN molecule, which exhibits multiple pKa values. Maximum degradation was observed at pH 8, likely due to optimal attractive interactions between the TCN molecule and the catalyst's surface at this pH, as shown in Table S5. Conversely, extreme acidic or basic conditions significantly reduced the degradation efficiency, likely due to reduced interaction between the catalyst and the pollutant molecule under these conditions.

3.6.4. Effect of catalysts dosage

The catalyst dosage is a critical factor in determining the practical efficacy and cost-related considerations when selecting catalysts for large-scale applications. In this experiment, the catalyst dosage was varied in the range of 50–200 mg L⁻¹ at an optimized pH of 8. The results are presented in Fig. 7 (e & f) and the corresponding rate constants are summarized in Table 2. At lower dosages, the catalyst is unable to engage a significant population of pollutant molecules due to insufficient surface area availability. Conversely, at an optimal higher dosage,

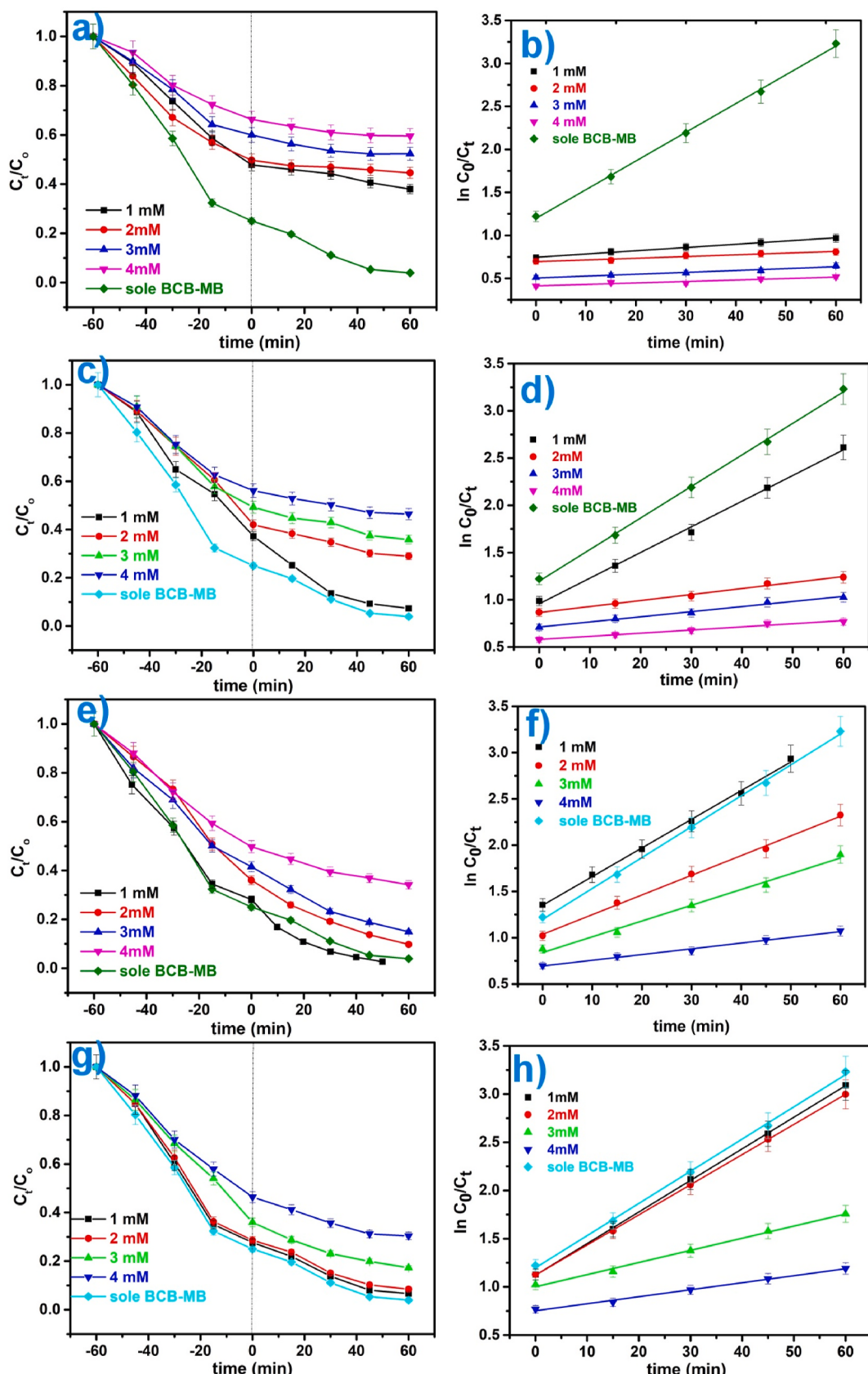
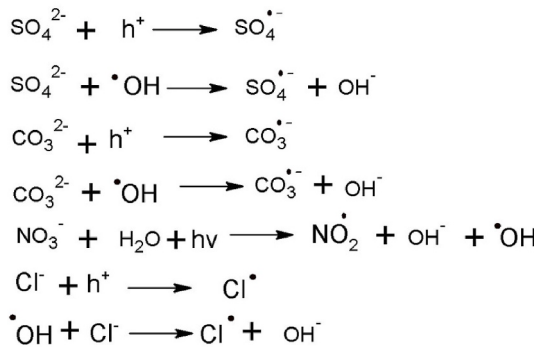


Fig. 8. (C_t/C_0) as a function of time and kinetic studies for effect of (a)–(b) SO_4^{2-} , (c)–(d) CO_3^{2-} , (e)–(f) NO_3^- and (g)–(h) Cl^- ions on photodegradation of TCN by BCB-MB.



Scheme 2. The interaction and transformation of Cl^- , CO_3^{2-} , NO_3^- and SO_4^{2-} with ROS.

the catalyst can interact effectively with a substantial number of pollutant molecules. However, beyond a certain threshold, the catalyst can act as a self-inhibitor. This phenomenon is primarily attributed to factors such as the obstruction of light penetration due to excessive

catalyst loading, which hinders the activation of photoinduced chemical reactions and consequently reduces the degradation rate. In the present study, a similar trend was observed: while lower catalyst dosages were less effective and the degradation efficiency increased with dosage, reaching a maximum of 96.2 % at 150 mg L⁻¹. Beyond this threshold, a reduction in degradation efficiency was noticed.

3.6.5. Effect of Cl^- , CO_3^{2-} , NO_3^- and SO_4^{2-} ions

The effect of various inorganic ions was studied in the concentration range of 1–4 mM, and the results are presented in Fig. 8. A significant inhibitory effect was observed in the case of SO_4^{2-} , even at a low concentration of 1 mM, followed by CO_3^{2-} at a concentration of 2 mM. This suppression of the photodegradation process was attributed to the interaction of SO_4^{2-} and CO_3^{2-} with reactive oxygen species (ROS) generated during the chain photochemical reaction, such as h^+ and $\cdot\text{OH}$, leading to their transformation into less reactive radicals, namely $\text{SO}_4^{\cdot-}$ and $\text{CO}_3^{\cdot-}$ as shown in Scheme 2. These radicals exhibit lower reactivity compared to $\cdot\text{OH}$, and beyond a certain threshold, they also compete for active sites on the catalyst surface. This competition results in the blocking of these sites, ultimately leading to an inhibitory effect

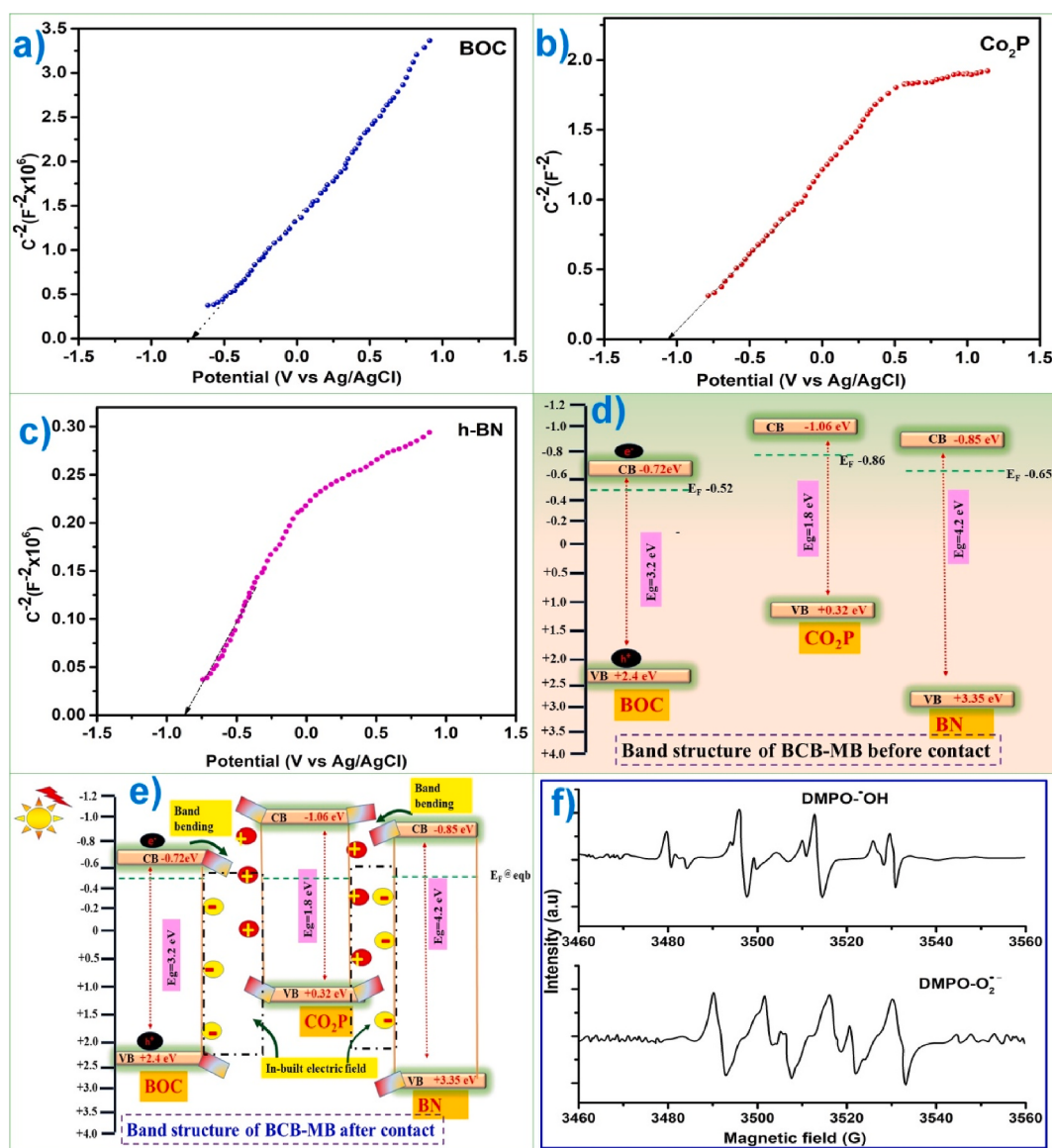


Fig. 9. (a)–(c) Mott-Schottky (M-S) plots for BOC, Co_2P , and h-BN respectively; (d) and (e) Band structure of BCB-MB before and after contact respectively; (f) ESR spectra of DMPO-•OH & and DMPO-O₂• adduct.

on the photodegradation process.

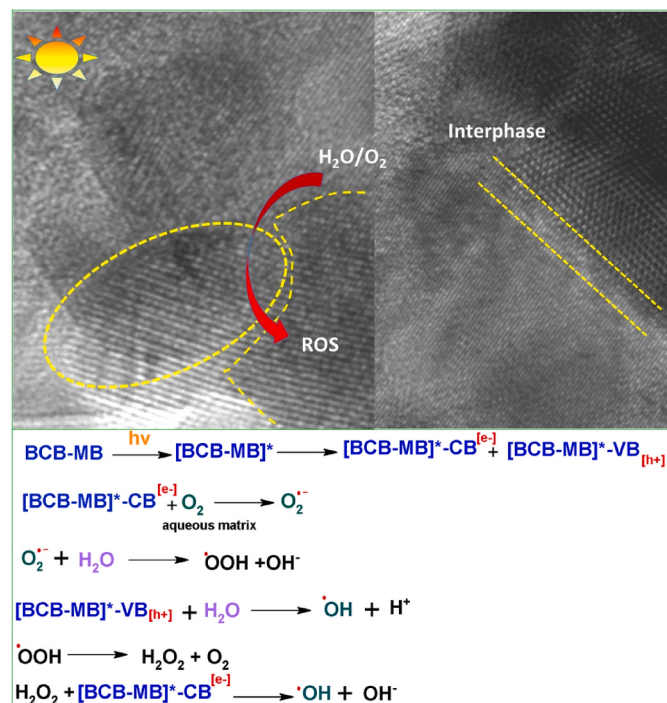
Conversely, NO_3^- ions at a lower concentration (1 mM) slightly enhanced the degradation process. This might be attributed to self-photolysis of NO_3^- in the presence of solar radiation, leading to the generation of $\bullet\text{OH}$ radical (Scheme 2). However, as the concentration increased beyond 1 mM, a retarding effect on photodegradation was observed, similar to other ions, with the maximum inhibition occurring at 4 mM. For Cl^- ions, at lower concentrations (1–2 mM), no significant impact on degradation was observed. However, beyond 3 mM, a noticeable retardation effect was detected, reaching its maximum at a concentration of 4 mM. At comparative high conc. the Cl^- ions also act as scavengers for reactive oxygen species (ROS), such as h^+ and $\bullet\text{OH}$, leading to their transformation into the less reactive $\text{Cl}\bullet$ radical as shown under (Scheme 2).

Scheme 2 illustrates the interaction between employed inorganic ions and reactive oxygen species (ROS), such as $\bullet\text{OH}$ and h^+ , which can alter the degradation pathway. The formation of secondary radicals like SO_4^\bullet , CO_3^\bullet , and $\text{Cl}\bullet$ through direct reactions with $\bullet\text{OH}$ or h^+ represents a significant scavenging process. These secondary radicals possess lower oxidative potential compared to $\bullet\text{OH}$, thereby diminishing the overall oxidation capacity of the system. Moreover, their relative stability in the reaction medium and tendency to block the active sites on the photocatalyst surface further reduce photocatalytic efficiency.

3.7. Working mechanism of photocatalyst

Fig. 9(a–c) depicts the Mott-Schottky (M-S) plots for BOC, Co_2P , and h-BN respectively. The positive slopes of the M-S plots confirm the n-type semiconductor behaviour of these photocatalysts. The flat band potentials (E_{FB}) determined from the intercepts of the plots were found to be -0.72 , -1.06 , and -0.85 V vs. Ag/AgCl for BOC, Co_2P , and h-BN, respectively. After conversion to the normal hydrogen electrode (NHE) scale, the corresponding potentials were taken as -0.52 , -1.06 , and -0.85 V vs. NHE. Generally, for n-type semiconductors, the Fermi level (E_F) is approximately equal to the flat band potential ($E_{FB} \approx E_F$), while the conduction band edge (E^{CB}) is typically located ~ 0.2 V more negative than the flat band potential (Majhi et al., 2020). Accordingly, the E^{CB} values for BOC, Co_2P , and h-BN were estimated to be -0.72 , -1.06 , and -0.85 eV, while the E_F values were taken as -0.52 , -1.06 , and -0.85 eV vs. NHE respectively. The E_{VB} were calculated from the UV-DRS analysis by applying the equation: $E_{VB} = E^{CB} + E_g$, which come out to be $+2.4$, $+0.32$ and $+3.35$ eV for BOC, Co_2P , and h-BN, respectively.

Fig. 9 (d) illustrates the band structure alignment of the BCB-MB photocatalyst (BOC/ Co_2P /h-BN) before contact. Upon the formation of interfacial contact between the ternary components, the Fermi levels of the individual counterparts tend to equilibrate, leading to band bending at the interfaces. Since the Fermi level of Co_2P is located at a more negative potential compared to BOC and h-BN, electron transfer occurs from Co_2P towards BOC and h-BN until Fermi level equilibrium is established. Consequently, a positive charge accumulates at the Co_2P interface, while negative charges develop at the BOC and h-BN interfaces. This charge redistribution induces upward band bending in Co_2P and downward band bending in BOC and h-BN, respectively, which ultimately lead to the in-built electric field at interfaces as schematically illustrated in **Fig. 9 (e)**. After the irradiation the in-built electric field force the photo induced electrons to migrate across the interface. Thus the photo excited electrons majorly accumulated at CB of BOC due to its lowermost E^{CB} then followed by h-BN. Now these free electrons are available further for the generation of various ROS and these migration possess enough potential for the formation of Superoxide radical (O_2^\bullet) ($\text{O}_2/\text{O}_2^\bullet = -0.33$ eV VS NHE) from the molecular O_2 . The photo excited electrons from the CB of BOC and h-BN get migrated to VB of Co_2P which suppress the charge recombination rates by preventing them to recombine back in the VB of BOC and h-BN. On the other sides VB of h-BN situated with more positive E_{VB} ($+3.4$ eV) followed by



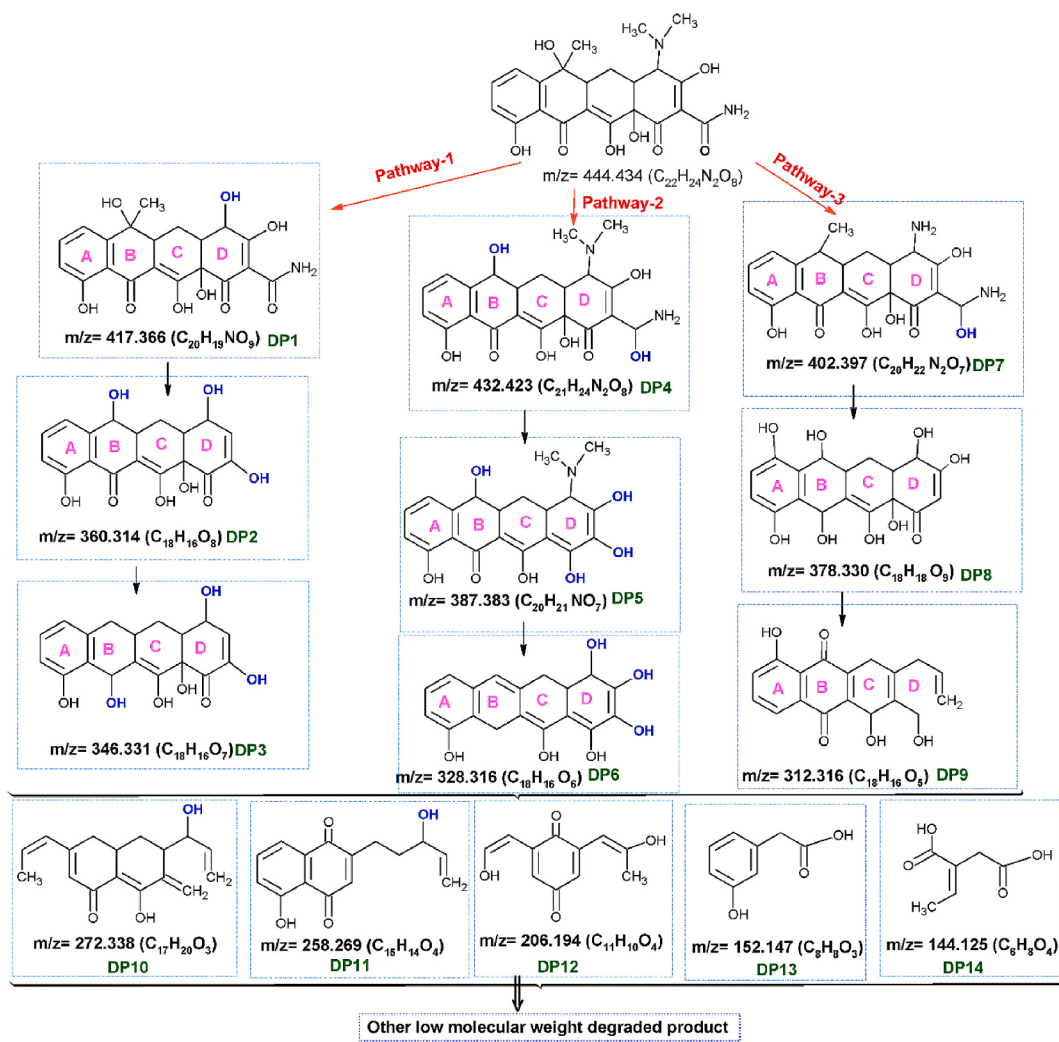
Scheme 3. Generation of ROS species after light exposure to BCB-MB.

BOC ($+2.4$ eV) and least in case of Co_2P ($+0.32$ eV). Thus the h^+ can migrates to VB of Co_2P and can generate the hydroxyl radical by oxidation reaction with H_2O ($\text{H}_2\text{O}/\bullet\text{OH} = +2.88$ eV Vs NHE) and $\text{OH}^-/\bullet\text{OH} = +1.99$ eV) (Tan et al., 2023).

Upon light irradiation, the built-in electric field drives the photo-generated electrons to migrate across the heterojunction interface. Consequently, the photoexcited electrons predominantly accumulate at the conduction band (CB) of BOC due to its lowest conduction band edge potential (ECB), followed by h-BN. These free electrons are subsequently available for the generation of various reactive oxygen species (ROS). Moreover, the migrated electrons possess sufficient reduction potential to facilitate the formation of superoxide radicals (O_2^\bullet) from molecular oxygen ($\text{O}_2/\text{O}_2^\bullet = -0.33$ eV vs NHE). Simultaneously, the photoexcited electrons in the CB of BOC and h-BN can migrate to the valence band (VB) of Co_2P , effectively suppressing the electron-hole recombination by preventing their recombination within the VB of BOC and h-BN. On the other hand, the valence band edge potentials (E_{VB}) of the materials follow the order: h-BN ($+3.4$ eV) $>$ BOC ($+2.4$ eV) $>$ Co_2P ($+0.32$ eV). Therefore, the photogenerated holes (h^+) can migrate from the VB of h-BN and BOC to the VB of Co_2P , where they can participate in oxidation reactions with H_2O ($\text{H}_2\text{O}/\bullet\text{OH} = +2.27$ eV vs NHE) or $\text{OH}^-/\bullet\text{OH} = +1.99$ eV vs NHE) to generate highly reactive hydroxyl radicals ($\bullet\text{OH}$). The above charge transfer mechanism and the generation of superoxide and hydroxyl radicals were further confirmed by electron spin resonance (ESR) spectroscopy. The corresponding results are presented in **Fig. 9 (f)**. The characteristic signals with intensity ratios of 1:1:1:1 and 1:2:2:1 were observed for the DMPO- O_2^\bullet and DMPO- $\bullet\text{OH}$ adducts, respectively.

3.8. LC-HRMS analysis of TCN and degradation pathway

Mass spectrometry (MS) was employed to determine the fate of photocatalytic degradation of TCN. The analysis was performed after 1 h and 2 h of the degradation experiment and the MS spectra are presented in **Fig. S5**. The results demonstrate that during the initial phase (1h) high molecular weight fragments were detected at $m/z = 444.434$ ($\text{C}_{22}\text{H}_{24}\text{N}_2\text{O}_8$), $m/z = 432.423$ ($\text{C}_{21}\text{H}_{24}\text{N}_2\text{O}_8$), $m/z = 417.366$



Scheme 4. Plausible TCN photodegradation mechanism by BCB-MB proposed on the basis of HR-MS analysis.

($C_{20}H_{19}NO_9$), $m/z = 402.392 (C_{22}H_{24}N_2O_8)$, $m/z = 387.383 (C_{20}H_{21}NO_7)$, $m/z = 378.330 (C_{18}H_{18}O_9)$, $m/z = 360.314 (C_{18}H_{16}O_8)$, $m/z = 346.331 (C_{18}H_{16}O_7)$, $m/z = 328.316 (C_{18}H_{16}O_6)$, and $m/z = 312.016 (C_{18}H_{16}O_5)$. Some of obtained fragments were found similar reported in previous studies (Yu et al., 2020; Du et al., 2021). Upon exposure of the catalyst-pollutant suspension to irradiation, the catalyst absorbs the appropriate light energy and undergoes various photochemical transformations, leading to the generation of reactive oxygen species (ROS), as illustrated in Scheme 3. These ROS further interact with the pollutant molecules, initiating the degradation process.

The overall degradation during the initial phase can be divided into three possible pathways, speculated based on the molecular fragments detected. The plausible degradation mechanism is depicted in Scheme 4 (Degradation Mechanism). In Pathway 1, degradation likely begins with the elimination of the $-N(CH_3)_2$ moiety from ring D, followed by hydroxylation, forming the degradation product DP1. In the subsequent step, the $-(CO)NH_2$ group detaches, and hydroxylation occurs again at the same ring, resulting in the formation of DP2. Further hydroxylation continues, leading to the formation of the degraded product DP3. Pathway 2 may begin with the demethylation at ring B, while the amide group at ring D undergoes hydroxylation and reduction simultaneously, and get transformed into the corresponding alcohol ($-CH(OH)NH_2$) forming DP4. In the subsequent step, hydroxylation occurs simultaneously at ring D, leading to the formation of the degraded product DP5. Further, the elimination of the $-N(CH_3)_2$ group from ring D, followed by hydroxylation at multiple positions, results in the formation of DP6.

Pathway 3 may initiate with the de-methylation at nitrogen in ring D, along with the reduction of $>C=O$ group (amide carbonyl) into a hydroxyl (-OH) group, forming DP7. In the next step, the loss of the $-NH_2$ group (directly attached to ring D) occurs, accompanied by the addition of a hydroxyl (-OH) group at the same position on ring D. Similarly, the loss of the $-CH(OH)NH_2$ group from the same ring leads to the formation of DP8. Subsequently, dehydroxylation at multiple sites, along with cleavage of the C-C bond in ring D, results in ring opening and the formation of DP9.

Throughout the degradation process, the pollutant molecules are continuously attacked by various reactive oxygen species (ROS). This leads to a series of chemical transformations, including hydroxylation, dehydroxylation, demethylation, and deamination. As the degradation experiment progresses into subsequent hours, the pollutant molecule further breaks down into lower molecular weight fragments, detected at $m/z = 272.338 (C_{17}H_{20}O_3)$, $m/z = 258.269 (C_{15}H_{14}O_4)$, $m/z = 206.194 (C_{11}H_{10}O_4)$, $m/z = 152.147 (C_8H_8O_3)$, and $m/z = 144.125 (C_6H_8O_4)$, as depicted in fig.S5 (b). The identified molecular fragments were enumerated under Table 3.

3.9. Treatment of real waste sample (RES) by BCB-MB

3.9.1. Analysis and identification of collected RES

Initially, the obtained effluent sample was analysed using LC-HR-MS to gain insight into the active pharmaceutical ingredients (APIs). The results of HR-MS analysis for RES were depicted in Fig. 10 (a). The

Table 3

Intermediate fragments identified after 2h of TCN degradation.

Transformed Intermediates	Molecular formula	m/z	Probable structure
DP10	C ₁₇ H ₂₀ O ₃	m/z= 272.338	
DP11	C ₁₅ H ₁₄ O ₄	m/z= 258.269	
DP12	C ₁₁ H ₁₀ O ₄	m/z= 206.194	
DP13	C ₈ H ₈ O ₃	m/z= 152.147	
DP14	C ₆ H ₈ O ₄	m/z= 144.125	

identification was based on the fragments obtained from the HR-MS analysis. HR-MS spectra of the effluent sample, showing major peaks at m/z = 59.110, m/z = 108.132, m/z = 176.254, m/z = 263.375, m/z = 279.161, m/z = 383.442, m/z = 411.451, m/z = 431.412, m/z = 494.495, m/z = 512.940, m/z = 528.940, and m/z = 557.597.

However, accurately predicting or identifying the exact residue of an API is highly challenging. Based on the detected fragments and their possible matches in fragment libraries, we can only speculate the presence of certain API residues. A review of the literature suggests that these molecular fragments indicate the presence of API residues from various pharmaceutical compounds, potentially belonging to analgesic, antibiotic and antimalarial drug classes. The peak at m/z = 263.375 confirms the presence of tramadol residues in the effluent, further supported by the peak at m/z = 176.254, which is associated with the core structure of tramadol. This peak corresponds to the phenylcyclohexanol moiety, formed by the cleavage of the amine and ether bond. Additionally, the presence of peaks at m/z = 108.132 and m/z = 59.110 further supports tramadol identification, as these are commonly observed signature fragments of the compound (Tambe et al., 2016; Shamai Yamin et al., 2024). Furthermore, the peak at m/z = 528.940 may be identified as the molecular ion fragment of lumefantrine. The peak at m/z = 512.940 can be attributed to the loss of an -OH group from the parent molecular ion. The peak at m/z = 494.495 is likely associated with the dechlorinated fragment arises due to loss of one chlorine from the parent fragment, while the peak at m/z = 279.161 may correspond to fragments of aromatic chlorinated fluorene rings

(Verbeken et al., 2011; Ateacha et al., 2019). Furthermore, the peak at m/z = 557.597 may be identified as cefpodoxime proxetil, corresponding to the protonated molecular ion. The peak at m/z = 431.412 possibly results from the loss of the proxetil ester moiety (-126 Da) from the parent molecular fragment. The peak at m/z = 411 can be attributed to the dehydrated cefpodoxime fragment (-18 Da; H₂O). Additionally, the peak at m/z = 383 may arise due to the loss of either a carbonyl or sulfur moiety from the dehydrated cefpodoxime fragment (Dubala et al., 2013; Li et al., 2014). The identified fragments were listed in Table S6. The other physico-chemical parameters such as COD, BOD, pH, Cl⁻ and F⁻ concentration were presented in Table S7.

3.9.2. Adsorption and photocatalytic treatment of RES

Fig. 10 (b) shows the UV-Vis spectra of RES which shows multiple absorption humps at; 243.3, 308, 352.2 and 440.9 nm. For the RES adsorption analysis 308 nm was taken as λ_{max} . BCB-MB catalyst shows a remarkable adsorption efficiency towards the RES as shown in Fig. 10 (c), about 78.45 % reduction was observed in the absorbance of selected λ_{max} after 2h of adsorption experiment. The UV-Vis spectra for adsorption experiment as a function of time was depicted in Fig. 5 (a). These adsorption results were obtained without any alteration to pH of the RES, the BCB-MB shows significant adsorption potential which demonstrate that composite possesses high potential for real scale water treatment on adsorption bases processes.

The efficiency of the BCB-MB toward photocatalytic removal was also studied for RES and results were demonstrated in Fig. 10 (d). The

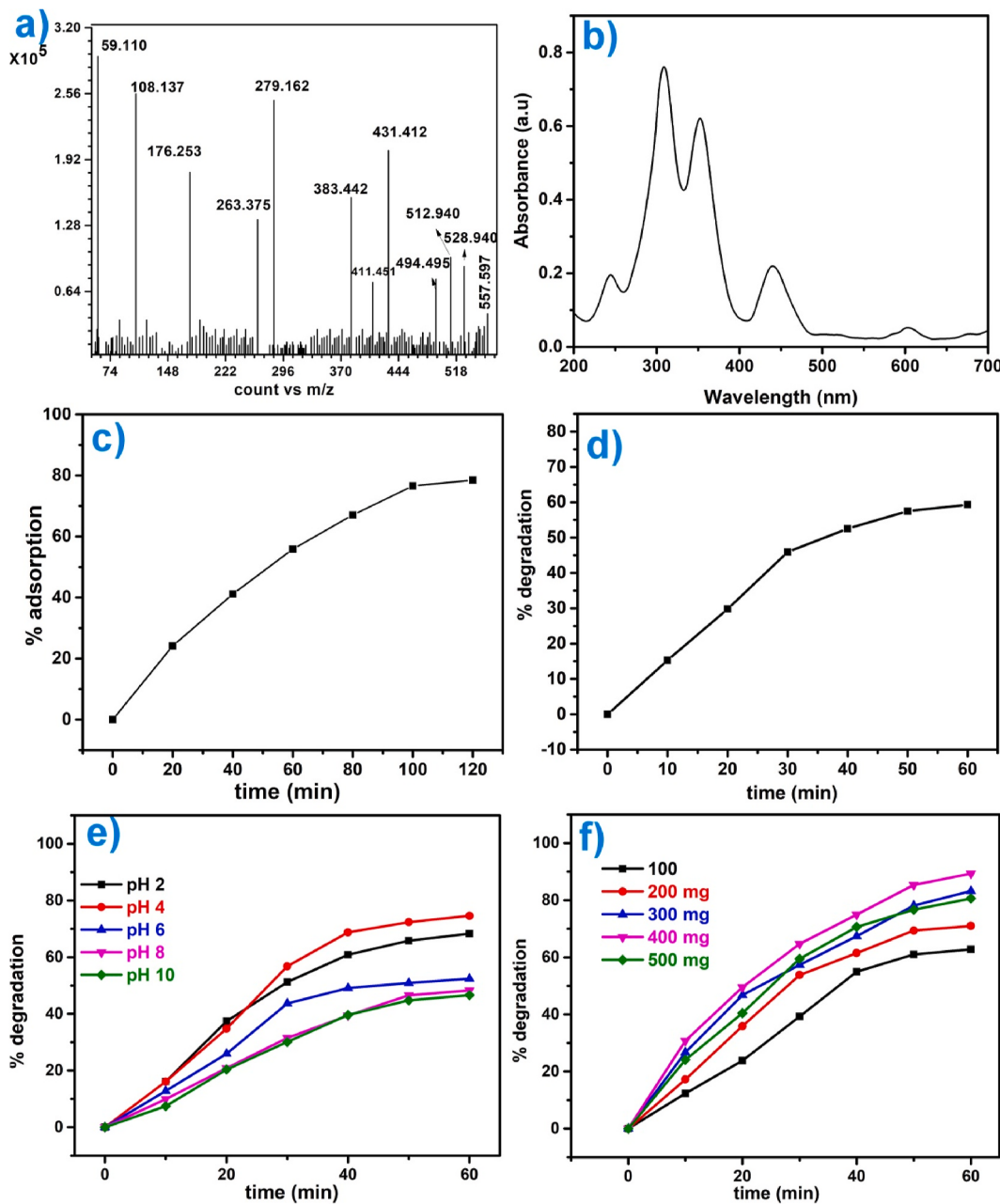


Fig. 10. a) HR-MS b) UV-Vis spectra of RES, c) % adsorption, d) % degradation of RES by BCB-MB, e) Effect of pH and f) catalysts dosage on photodegradation of RES.

results illustrates that catalysts is able to degrade about 59.3 % of RES. The time dependent UV-Vis spectra of RES during the course of degradation experiment is presented in Fig. 5 (b). If we compare the photo-degradation results obtained for TCN and RES, BCB-MB shows poor degradation efficiency for RES as compared to TCN at natural condition. Various factor may contributes for this impact as RES have multiple API residues that may have various interaction variation with the catalysts surface. Another factor may be the presence of various inorganic ions that may have impact on the degradation process. Thus the optimization parameters further explored in the proceeding section.

3.9.3. Effect of pH and catalysts dosage

The pH of RES was observed to be slightly acidic ($\text{pH} = 6.2$). The effect of pH on the degradation of RES by the BCB-MB catalyst was investigated over a pH range of 2–10. The results are shown in Fig. 10 (e), with the observed degradation efficiencies as follows: pH 4 (74.6 %),

pH 2 (68.3 %), pH 6 (52.4 %), pH 8 (48.3 %), and pH 10 (46.6 %). This trend can be attributed to two major factors. First, the strong electrostatic interactions at lower pH levels between the catalyst surface ($\text{PZC} = 8.3$) and RES play a crucial role. The API residue may exist in an anionic form by donating H^+ , allowing it to exist as its conjugate base at lower pH. Second, the acid-base reactions occurring on the catalyst surface proceed rapidly, further influencing the degradation process.

In this experiment, the catalyst dosage was varied within the range of $100\text{--}500 \text{ mg L}^{-1}$ at a controlled pH of 4. The results are presented in Fig. 10 (f). At lower dosages, the catalyst is unable to interact effectively with a significant fraction of the API residues present in the RES sample, due to limited surface area availability. In contrast, at an optimal dosage of 400 mg L^{-1} , the catalyst efficiently engages with a larger proportion of API residues, leading to the degradation of 89.3 % of the RES. HR-MS analysis was performed after 1 h of the RES photodegradation experiment ($\text{pH } 2$, catalyst dosage: 400 mg L^{-1}) using the BCB-MB

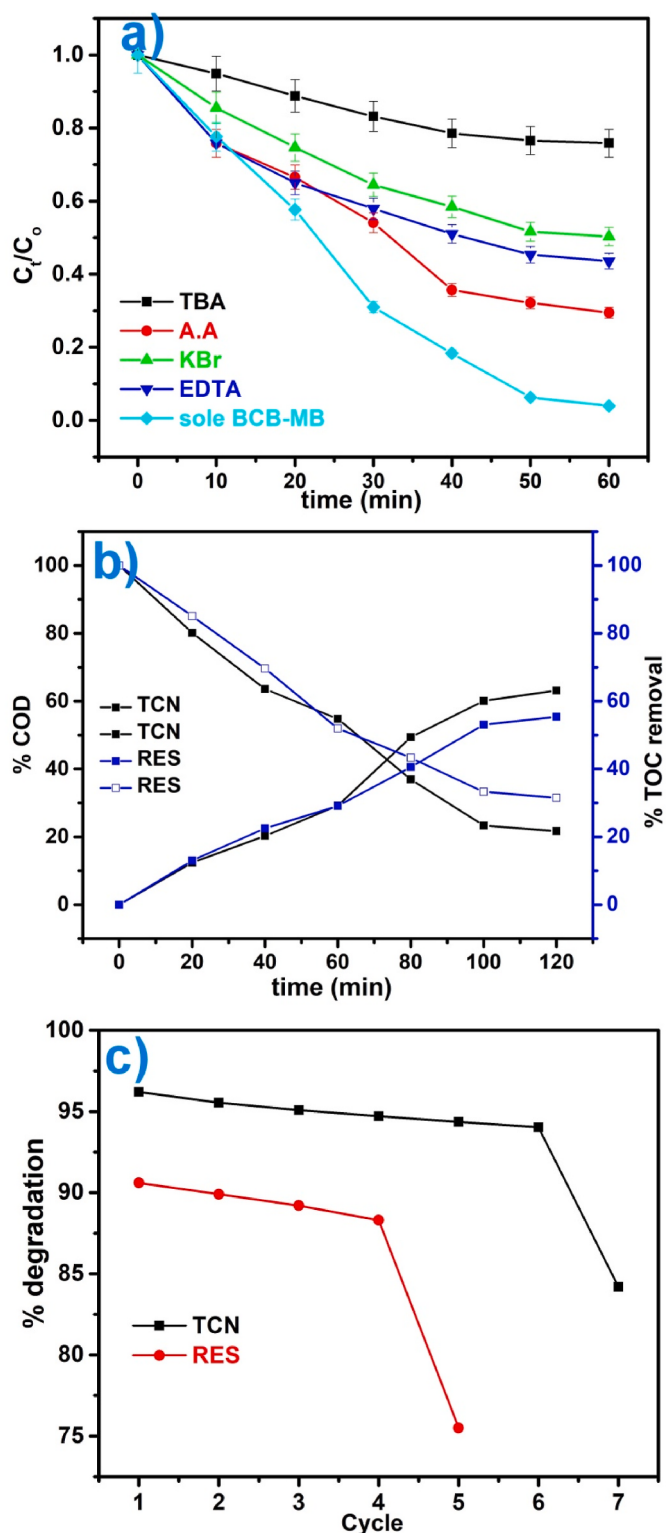


Fig. 11. a) Effect of employed radical scavenger on TCN degradation and b) COD & TOC analysis after 2h of TCN & RES photodegradation and c) Recyclability analysis of BCB-MB.

photocatalyst. The major peaks corresponding to high molecular weight fragments (m/z) either disappeared or were significantly reduced in intensity, while new peaks at lower m/z values emerged, as illustrated in Fig. S6. These results indicate that the BCB-MB photocatalyst exhibits remarkable potential for real-scale wastewater treatment applications.

Based on the analysis of pH and catalyst dosage, it can be inferred

that photocatalysts exhibit distinct behaviours during the degradation process in simulated versus real wastewater conditions, using tetracycline (TCN) and real effluent sample (RES) as model pollutants. The pH-dependent study revealed that maximum degradation of TCN occurred at pH 8, achieving 90.6 % efficiency, whereas RES exhibited its highest degradation at pH 4, with 74.6 % efficiency. This discrepancy highlights that optimal parameters determined under simulated conditions may not be directly translatable to real-world wastewater treatment scenarios. A comparable trend was observed with respect to catalyst dosage: while only 150 mg L⁻¹ of catalyst was sufficient to achieve 96.2 % degradation of TCN, a significantly higher dosage of 400 mg L⁻¹ was required to achieve 89.3 % degradation of RES within the same time frame. These findings underscore the critical need to evaluate photocatalyst performance under realistic conditions, as promising results in simulated environments do not necessarily guarantee equivalent efficacy in real-scale applications.

3.10. Identification of major active radicle species responsible for the photodegradation, COD, TOC and recyclability analysis

The band structure of the BCB-MB photocatalyst clearly indicates that it possesses sufficient potential to generate various reactive oxygen species (ROS). However, it provides limited insight into which specific ROS plays the dominant role in the degradation process. To gain this information, a radical scavenging experiment was conducted using 4 mM of each of the following scavengers: tert-butyl alcohol (TBA), ascorbic acid (AA), potassium bromide (KBr), and ethylenediaminetetraacetic acid (EDTA), which are known to selectively scavenge $\bullet\text{OH}$, $\text{O}_2\bullet^-$, free electrons (e^-), and holes (h^+), respectively. The analysis, as presented in Fig. 11 (a) shows that the degradation process was most significantly quenched in the presence of tert-butyl alcohol (TBA), followed by ascorbic acid (AA), with the percentage degradation decreasing to 24.4 % and 38.4 %, respectively. This indicates that hydroxyl radicals ($\bullet\text{OH}$) play the most dominant role in the degradation process, followed by superoxide radicals ($\text{O}_2\bullet^-$). Furthermore, the presence of potassium bromide (KBr) and ethylenediaminetetraacetic acid (EDTA) also resulted in a marked reduction in degradation efficiency, suggesting that electrons (e^-) and holes (h^+) contribute significantly as well. Although e^- and h^+ may not directly degrade the pollutant, they likely facilitate the formation of other reactive oxygen species, thereby playing an indirect yet critical role in the overall photocatalytic mechanism. COD (Chemical Oxygen Demand) and TOC (Total Organic Carbon) analyses were conducted after 2 h of degradation, and the results are presented in Fig. 11 (b). The analysis revealed a 63.4 % & 55.3 % reduction in TOC and a 79.2 % & 68.4 % decrease in COD, was observed in case of TCN and RES indicating substantial degradation of pollutants.

The recyclability of a photocatalyst is an important parameter that determines its cost-related impact, particularly when considered for large-scale applications. Therefore, under identical conditions, reusability experiments were conducted for the degradation of both TCN and RES. After each experimental run, the photocatalyst was magnetically separated and washed with a 1:1 (v/v) ethanol–water mixture to remove any residual pollutants adhered to the catalyst surface, followed by drying at 70 °C. The recycled catalyst was then reused for the next experimental cycle. As shown in Fig. 11 (c), the BCB-MB photocatalyst exhibited only a slight decrease in TCN degradation efficiency, from 96.2 % to 94.4 %, up to the sixth cycle. However, in the seventh cycle, the efficiency dropped more noticeably to 84.2 %. In the case of RES degradation, the catalyst remained reusable for up to four consecutive cycles (with efficiency decreasing from 90.6 % to 88.3 %); however, in the fifth cycle, the degradation efficiency declined to 77.5 %. These results indicate that under realistic conditions, the catalyst maintains good reusability up to four cycles.

Table 4

Comparison of BCB/MB performance with previous literature.

TCN Degradation						
Catalyst	Initial conc. of TCN (mg/L)	Dosage (g/L)	Light source	Reaction time (min)	Kinetic constant/% degradation	Ref
Pt/TiO ₂	20	0.33	300 W Xe lamp	30	0.09196	Li et al. (2024b)
PVDF/rGO/CuO	20	0.02	Natural solar light	90	1.141	Behera et al. (2024)
W ₁₈ O ₄₉ /Bi ₂ O ₃	20	0.02	300 W Xe lamp	40	97	Tie et al. (2025)
Bi ₂ Sn ₂ O ₇ /Bi ₄ O ₇	10	0.030	300 W Xe lamp	60	0.053	Zhen et al. (2024)
BCB/MB	60	0.150	500 W Xe lamp	60	0.0334	Present work

Real waste water treatment catalysts						
catalysts	Effluents source	Dosage (g/L)	Light source	Reaction time	Efficiency (%)	Ref
TiO ₂ /PAC	slaughterhouse and urban wastewater	1	40 w UVA lamp	120	77 to 100 for the slaughterhouse effluent & 61–89 for the wastewater	Moles et al. (2024)
PES/TiO ₂ -GO	textile	–	UV lamp	60	96	Bhattacharyya et al. (2025)
TiO ₂ -LC	municipal wastewater treatment plant	–	CRI-LED	180	54	Kubiak (2025)
CV/HBN	dye factory	0.8	300 W Xe lamp	60	90.2	Sasikumar and Rajaram (2024)
BCB/MB	Pharmaceutical	0.4	500 W Xe lamp	60	89.3	Present work

3.11. Comparison with existing literature

To evaluate the photocatalytic efficiency of the synthesized BCB-MB composite, its performance was compared with several reported photocatalysts for tetracycline (TCN) degradation and real wastewater treatment as shown in Table 4. BCB/MB demonstrating superior or competitive performance compared to many reported systems. For instance, Pt/TiO₂ achieved $\sim 0.09196 \text{ min}^{-1}$ rate constant under a 300 W Xe lamp in 30 min, while PVDF/rGO/CuO, though highly efficient under natural solar light, required 90 min for similar performance. Other catalysts such as W₁₈O₄₉/Bi₂O₃ and Bi₂Sn₂O₇/Bi₄O₇ also showed notable activity but longer reaction times. When applied to real wastewater, the BCB-MB system also outperformed or matched the reported efficiencies of other photocatalysts. For example, TiO₂/PAC exhibited 77–100 % removal for slaughterhouse effluent but only 61–89 % for municipal wastewater. Likewise, TiO₂-LC under CRI-LED light required 180 min to reach 54 % efficiency. In contrast, the BCB-MB catalyst maintained high degradation performance even with complex effluents, indicating its versatile potential for both synthetic antibiotic and real wastewater remediation under visible light irradiation.

4. Conclusion

The BCB-MB composite, comprising boron nitride (BN), bismuth oxychloride (BOC), cobalt phosphide (Co₂P), and magnetic biochar, exhibited superior performance for the removal of tetracycline (TCN) under mildly basic conditions (pH 8), achieving 96.2 % degradation within 60 min at a catalyst dosage of 150 mg L⁻¹. The composite also demonstrated a high adsorption capacity, with approximately 92.2 % of TCN being adsorbed. Interference studies revealed that sulfate and carbonate ions significantly suppressed the degradation efficiency. The exceptional photocatalytic activity of the composite is attributed to its enhanced optical properties, including efficient charge separation, strong visible-light absorption, and suppressed electron-hole recombination and its well-aligned band structure. The S-scheme heterojunction mechanism was proposed for the working of the BCB-MB catalyst, wherein the built-in electric field facilitates effective charge transfer and promotes the generation of reactive oxygen species (ROS) under light irradiation. The hydroxyl radicals ($\bullet\text{OH}$) were identified as the

dominant species driving the photodegradation of pollutants. Notably, the catalyst also displayed excellent performance in the treatment of real wastewater samples, achieving 90.6 % degradation under acidic conditions (pH 4) with a catalyst dosage of 400 mg L⁻¹. BCB-MB found reusable up to four cycles for real effluent treatment. Compared to previously reported photocatalysts, the BCB-MB system exhibited competitive or superior performance, with degradation efficiencies typically ranging between 54 % and 97 % under varying conditions in the literature. Similarly, for real wastewater treatment, previously reported efficiencies ranged from 54 % to 96 % depending on the effluent type, light source, and operating time, indicating the robustness and versatility of BCB-MB across diverse environmental scenarios. This study also underscores the critical insight that photocatalyst behaviour under controlled laboratory conditions may not fully replicate its performance in real-world applications. Furthermore, high-resolution mass spectrometry (HR-MS) was employed to elucidate the degradation pathway, and a plausible mechanism was proposed based on the identified intermediates. By aligning well with or exceeding established benchmarks, the findings position BCB-MB as a promising multifunctional photocatalyst for practical environmental remediation.

CRediT authorship contribution statement

Pooja Dhiman: Writing – review & editing, Methodology, Data curation. **Manisha Dhiman:** Writing – review & editing, Validation, Project administration, Funding acquisition. **Arush Sharma:** Software, Resources, Formal analysis. **Manickam Selvaraj:** Funding acquisition, Data curation. **Mohammed A. Assiri:** Formal analysis, Data curation. **Ajay Kumar:** Writing – original draft, Supervision, Project administration, Investigation, Conceptualization.

Declaration of competing interest

The authors declare that they have no known competing financial interests or personal relationships that could have appeared to influence the work reported in this paper.

Acknowledgements

The authors sincerely express their gratitude to the H.P. Council for Science, Technology & Environment (HIMCOSTE) for providing financial support for this work through the HIMCOSTE research project No. STC/F(8)-2/2021 (R&D)/21-22-2040.

The authors also extend their appreciation to the Deanship of Scientific Research and Graduate Studies at King Khalid University for funding this work through the Large Project number R.G.P. 2/690/46 and the authors acknowledge the Research Center for Advanced Materials (RCAMS) at King Khalid University, Saudi Arabia for their valuable technical support.

Appendix A. Supplementary data

Supplementary data to this article can be found online at <https://doi.org/10.1016/j.jenvman.2025.126676>.

Data availability

Data will be made available on request.

References

- Abid, M.F., Alwan, G.M., Abdul-Ridha, L.A., 2016. Study on catalytic wet air oxidation process for phenol degradation in synthetic wastewater using trickle bed reactor. SpringerMF Abid, GM Alwan, LA Abdul-RidhaArabian J. Sci. Eng. 2016•Springer 41, 2659–2670. <https://doi.org/10.1007/S13369-016-2171-X>.
- Ahmed, Y., Zhong, J., Yuan, Z., Guo, J., 2022. Roles of reactive oxygen species in antibiotic resistant bacteria inactivation and micropollutant degradation in Fenton and photo-Fenton processes. *J. Hazard. Mater.* 430, 128408. <https://doi.org/10.1016/J.JHAZMAT.2022.128408>.
- Aktas, K., Liu, H., Eskicioglu, C., 2024. Treatment of aqueous phase from hydrothermal liquefaction of municipal sludge by adsorption: Comparison of biochar, hydrochar, and granular activated carbon. *J. Environ. Manag.* 356, 120619. <https://doi.org/10.1016/J.JENVMAN.2024.120619>.
- Ateacha, D.N., Kuhlmann, C., Engelhard, C., 2019. Rapid screening of antimalarial drugs using low-temperature plasma desorption/ionization Orbitrap mass spectrometry. *Anal. Methods* 11, 566–574. <https://doi.org/10.1039/c8ay02538j>.
- Ayiania, M., Smith, M., Hensley, A.J.R., Scudiero, L., McEwen, J.S., Garcia-Perez, M., 2020. Deconvoluting the XPS spectra for nitrogen-doped chars: an analysis from first principles. *Carbon N. Y.* 162, 528–544. <https://doi.org/10.1016/J.CARBON.2020.02.065>.
- Behler, S.A., Subhadarshini, A., Bhuyan, S.S., Nanda, B., Achary, P.G.R., 2024. PVDF/rGO/CuO nanocomposites: a robust platform for solar-driven tetracycline photodegradation. *Inorg. Chem. Commun.* 160, 111995. <https://doi.org/10.1016/J.INOCHE.2023.111995>.
- Ben Mbarek, W., Escoda, L., Saurina, J., Pineda, E., Alminderej, F.M., Khitouni, M., Sunol, J.J., 2022. Nanomaterials as a sustainable choice for treating wastewater: a review. *Materials* 15, 8576. <https://doi.org/10.3390/MA15238576>, 8576 15.
- Bhattacharyya, S., Heran, M., Chakraborty, S., Calabro, V., Algieri, C., 2025. Enhancing the efficiency of photocatalytic membrane reactors for textile effluent remediation. *Sep. Purif. Technol.* 375, 133714. <https://doi.org/10.1016/J.SEPPUR.2025.133714>.
- Bi, Z., Wang, W., Zhao, L., Wang, X., Xing, D., Zhou, Y., Lee, D.J., Ren, N., Chen, C., 2024. The generation and transformation mechanisms of reactive oxygen species in the environment and their implications for pollution control processes: a review. *Environ. Res.* 260, 119592. <https://doi.org/10.1016/J.ENVR.2024.119592>.
- Cai, H., Zhang, H., Gao, N., Fang, Y., Xie, X., Fang, Y., Chen, G., 2024. Novel N-ZnO/p-BN adsorption-photocatalytic composites with interfacial bonding for efficient synergistic degradation of pollutants in water. *Appl. Surf. Sci.* 677, 161060. <https://doi.org/10.1016/JAPSUSC.2024.161060>.
- Chandek, M., Thakur, M., Sharma, A., Pathania, D., Kumar, A., Singh, L., 2022. Chlorophyll sensitized (BiO)2CO3/CdWO4/rGO nano-hybrid assembly for solar assisted photo-degradation of chloroxazone. *Chemosphere* 305, 135472. <https://doi.org/10.1016/J.CHEMOSPHERE.2022.135472>.
- Chen, L., Navya, B.S., Di Dong, C., 2024. Construction of MoS₂/BN nanohybrids with enhanced photocatalytic performance for RhB and TC degradation. *J. Phys. Chem. Solid* 193, 112170. <https://doi.org/10.1016/J.JPCS.2024.112170>.
- Cheng, H., Huang, B., Yang, K., Wang, Z., Qin, X., Zhang, X., Dai, Y., 2010. Facile template-free synthesis of Bi2O2CO3 hierarchical microflowers and their associated photocatalytic activity. *ChemPhysChem* 11, 2167–2173. <https://doi.org/10.1002/cphc.200901017>.
- Choi, J., Reddy, D.A., Kim, T.K., 2015. Enhanced photocatalytic activity and anti-photocorrosion of AgI nanostructures by coupling with graphene-analogue boron nitride nanosheets. *Ceram. Int.* 41, 13793–13803. <https://doi.org/10.1016/J.CERAMINT.2015.08.062>.
- Cocker, D., Birgand, G., Zhu, N., Rodriguez-Manzano, J., Ahmad, R., Jambo, K., Levin, A., Holmes, A., 2024. Healthcare as a driver, reservoir and amplifier of antimicrobial resistance: opportunities for interventions. *Nat. Rev. Microbiol.* 22, 636–649. <https://doi.org/10.1038/s41579-024-01076-4>, 2024 2210.
- de Ilurdoz, M.S., Sadhwani, J.J., Reboso, J.V., 2022. Antibiotic removal processes from water & wastewater for the protection of the aquatic environment - a review. *J. Water Process Eng.* 45, 102474. <https://doi.org/10.1016/J.JWPE.2021.102474>.
- Dong, C., Fang, W., Yi, Q., Zhang, J., 2022. A comprehensive review on reactive oxygen species (ROS) in advanced oxidation processes (AOPs). *Chemosphere* 308, 136205. <https://doi.org/10.1016/J.CHEMOSPHERE.2022.136205>.
- Du, Z., Feng, L., Guo, Z., Yan, T., Hu, Q., Lin, J., Huang, Y., Tang, C., Fang, Y., 2021. Ultrathin h-BN/Bi2MoO6 heterojunction with synergistic effect for visible-light photocatalytic tetracycline degradation. *J. Colloid Interface Sci.* 589, 545–555. <https://doi.org/10.1016/J.JCIS.2021.01.027>.
- Du, Y., Lu, T., Li, X., Liu, Y., Sun, W., Zhang, S., Cheng, Z., 2022. High-efficient piezocatalytic hydrogen evolution by centrosymmetric Bi2Fe4O9 nanoplates. *Nano Energy* 104, 107919. <https://doi.org/10.1016/J.NANOEN.2022.107919>.
- Dubala, A., Nagarajan, J.S.K., Vimal, C.S., George, R., 2013. Simultaneous quantification of cefpodoxime proxetil and clavulanic acid in human plasma by LC-MS using solid phase extraction with application to pharmacokinetic studies. *J. Chromatogr. B* 921–922, 49–55. <https://doi.org/10.1016/J.JCHROMB.2013.01.018>.
- Butta, V., Sharma, S., Raizada, P., Khan, A.A.P., Asiri, A.M., Nadda, A., Singh, P., Van Le, Q., Huang, C.W., Nguyen, D.L.T., Pansambal, S., Nguyen, V.H., 2021. Recent advances and emerging trends in (BiO)2CO3 based photocatalysts for environmental remediation: a review. *Surf. Interfaces* 25, 101273. <https://doi.org/10.1016/J.SURFIN.2021.101273>.
- Feng, C., Tang, L., Deng, Y., Zeng, G., Wang, J., Liu, Y., Chen, Z., Yu, J., Wang, J., 2019. Enhancing optical absorption and charge transfer: synthesis of S-doped h-BN with tunable band structures for metal-free visible-light-driven photocatalysis. *Appl. Catal. B Environ.* 256, 117827. <https://doi.org/10.1016/J.APCATB.2019.117827>.
- Han, X., Yang, J., Zhao, H., Wang, Q., Ruan, F., Shang, W., Bao, J., Ma, Y., 2025. Multichannel charge transfer in TiO₂/CdS/Co₂P ternary heterostructure for enhanced photocatalytic hydrogen evolution. *Int. J. Hydrogen Energy* 117, 86–96. <https://doi.org/10.1016/J.IJHYDENE.2025.03.179>.
- Huang, S., Xu, Y., Xie, M., Xu, H., He, M., Xia, J., Huang, L., Li, H., 2015. Synthesis of magnetic CoFe2O4/g-C3N4 composite and its enhancement of photocatalytic ability under visible-light. *Colloids Surfaces A Physicochem. Eng. Asp.* 478, 71–80. <https://doi.org/10.1016/J.J.COLSURFA.2015.03.035>.
- Hughes, A.E., Easton, C.D., Gengenbach, T.R., Biesinger, M.C., Laleh, M., 2024. Interpretation of complex x-ray photoelectron peak shapes. I. Case study of Fe 2p3/2 spectra. *J. Vac. Sci. Technol. A* 42, 53205. <https://doi.org/10.1116/6.0003804/3309427>.
- Ighalo, J.O., Rangabhashiyam, S., Dulta, K., Umeh, C.T., Iwuozer, K.O., Aniagor, C.O., Eshiemogie, S.O., Iwuchukwu, F.U., Igwegbe, C.A., 2022. Recent advances in hydrochar application for the adsorptive removal of wastewater pollutants. *Chem. Eng. Res. Des.* 184, 419–456.
- Ilić, M., Haegel, F.H., Lolić, A., Nedić, Z., Tostic, T., Ignjatović, I.S., Linden, A., Jablonowski, N.D., Hartmann, H., 2022. Surface functional groups and degree of carbonization of selected chars from different processes and feedstock. *PLoS One* 17. <https://doi.org/10.1371/journal.pone.0277365>.
- Ivanova, M.N., Vorotnikov, Y.A., Plotnikova, E.E., Marchuk, M.V., Ivanov, A.A., Asanov, I.P., Tsygankova, A.R., Grayfer, E.D., Fedorov, V.E., Shestopalov, M.A., 2020. Hexamolybdenum clusters supported on exfoliated h-BN nanosheets for photocatalytic water purification. *Inorg. Chem.* 59, 6439–6448. https://doi.org/10.1021/ACS.INORGCHEM.0C00528 SUPPL_FILE/IC0C00528 SI_001.PDF.
- Jaiswal, A.K., Maji, B., Kumar, M., Maity, J., 2024. Structure-property correlation of a newly synthesized 6351Al/Body-Centered tetragonal boron nitride composite. *J. Mater. Eng. Perform.* 33, 7164–7193. <https://doi.org/10.1007/S11665-023-08838-W/METRICS>.
- Ji, X., Guo, Y., Hua, S., Li, H., Zhang, S., 2020. Interaction-determined sensitization photodegradation of dye complexes by boron nitride under visible light irradiation: experimental and theoretical studies. *New J. Chem.* 44, 9238–9247. <https://doi.org/10.1039/donj01387k>.
- Jia, Y., Li, S., Gao, J., Zhu, G., Zhang, F., Shi, X., Huang, Y., Liu, C., 2019. Highly efficient (BiO)2CO3-BiO2-x-graphene photocatalysts: Z-Scheme photocatalytic mechanism for their enhanced photocatalytic removal of NO. *Appl. Catal. B Environ.* 240, 241–252. <https://doi.org/10.1016/J.APCATB.2018.09.005>.
- Jiang, D., Ma, W., Zhou, Y., Xing, Y., Quan, B., Li, D., 2019. Coupling Co₂P and Co₃P nanoparticles with copper ions incorporated Co₉₈ nanowire arrays for synergistically boosting hydrogen evolution reaction electrocatalysis. *J. Colloid Interface Sci.* 550, 10–16. <https://doi.org/10.1016/J.JCIS.2019.04.080>.
- Ji, A., Wu, L., Lu, J., Feng, B., Che, G., Guan, R., Zhang, Y., Liu, C., Yu, J., Sun, T., 2024. BiOBr/Bi2O2CO3 heterojunction photocatalyst for the degradation of tetracycline. *ACS Appl. Nano Mater.* 7, 12722–12733. https://doi.org/10.1021/ACSNM.4C01247 SUPPL_FILE/AN4C01247_SI_001.PDF.
- Khan, N.A., López-Maldonado, E.A., Majumder, A., Singh, S., Varshney, R., López, J.R., Méndez, P.F., Ramamurthy, P.C., Khan, M.A., Khan, A.H., Mubarak, N.M., Amhad, W., Shamshuddin, S.Z.M., Aljundi, I.H., 2023. A state-of-art-review on emerging contaminants: environmental chemistry, health effect, and modern treatment methods. *Chemosphere* 344, 140264. <https://doi.org/10.1016/J.CHEMOSPHERE.2023.140264>.
- Kubiak, A., 2025. A scalable IoT-controlled photocatalytic system for pharmaceutical removal in real wastewater treatment applications. *Chem. Eng. J.* 518, 164709. <https://doi.org/10.1016/J.CEJ.2025.164709>.
- Kumar Bhoi, N., Singh, H., Pratap, S., 2020. Synthesis and characterization of zinc oxide reinforced aluminum metal matrix composite produced by microwave sintering. *J. Compos. Mater.* 54, 3625–3636. <https://doi.org/10.1177/0021998320918646>.

- Kumar, A., Kumar, A., Sharma, G., Naushad, M., Stadler, F.J., Ghfar, A.A., Dhiman, P., Saini, R.V., 2017a. Sustainable nano-hybrids of magnetic biochar supported g-C₃N₄/FeVO₄ for solar powered degradation of noxious pollutants- Synergism of adsorption, photocatalysis & photo-ozonation. *J. Clean. Prod.* 165, 431–451. <https://doi.org/10.1016/j.jclepro.2017.07.117>.
- Kumar, A., Shalini, Sharma, G., Naushad, M., Kumar, A., Kalia, S., Guo, C., Mola, G.T., 2017b. Facile hetero-assembly of superparamagnetic Fe₃O₄/BiVO₄ stacked on biochar for solar photo-degradation of methyl paraben and pesticide removal from soil. *J. Photochem. Photobiol. Chem.* 337, 118–131. <https://doi.org/10.1016/J.JPHOTOCHEM.2017.01.010>.
- Kumari, S., Sharma, A., Dhiman, P., Thakur, M., Aloui, Z., Selvaraj, M., Kumar, A., 2025. Strategic synthesis of biowaste-derived magnetic hydrochar for adsorption and photocatalytic removal of Chloryrifos herbicides from simulated wastewater. *Mater. Sci. Eng. B* 314, 118009. <https://doi.org/10.1016/J.MSEB.2025.118009>.
- Kwoka, M., Comini, E., Zappa, D., Szuber, J., 2022. Flower-like ZnO nanostructures local surface morphology and chemistry. *Nanomaterials* 12. <https://doi.org/10.3390/nano12152666>.
- Li, J., Zhang, D., Hu, C., 2014. Characterization of impurities in cefpodoxime proxetil using LC-MSn. *Acta Pharm. Sin. B* 4, 322–332. <https://doi.org/10.1016/J.APSB.2014.06.007>.
- Li, Y., Ma, S., Xu, S., Fu, H., Li, Z., Li, K., Sheng, K., Du, J., Lu, X., Li, X., Liu, S., 2020. Novel magnetic biochar as an activator for peroxymonosulfate to degrade bisphenol A: emphasizing the synergistic effect between graphitized structure and CoFe2O4. *Chem. Eng. J.* 387, 124094. <https://doi.org/10.1016/J.CEJ.2020.124094>.
- Li, Y., Wu, S., Liang, F., Lv, G., Tian, Y., Zhang, H., Liu, Y., Liu, G., 2024a. Rod-like h-BN modified low carbon Al₂O₃-C refractory and its high-temperature service performances. *J. Eur. Ceram. Soc.* 44, 1825–1835. <https://doi.org/10.1016/J.JEURCERAMSOC.2023.10.021>.
- Li, D., Li, Y., Liao, D., Cao, M., Zhang, L., Zhang, S., Chen, L., Chen, Y., Wang, H., Qi, J., You, F., 2024b. Enhanced light harvesting ability in hollow Pt/TiO₂ nanoreactor for boosting tetracycline photodegradation. *Prog. Nat. Sci. Mater. Int.* 34, 767–775. <https://doi.org/10.1016/J.JPNSC.2024.07.005>.
- Liang, R., Wang, Y., Qin, C., Chen, X., Ye, Z., Zhu, L., 2021. P-type cobalt phosphide composites (Co₃P₂P) decorated on titanium oxide for enhanced noble-metal-free photocatalytic H₂Evolution activity. *Langmuir* 37, 3321–3330. https://doi.org/10.1021/ACS.LANGMUIR.0C03362/SUPPL_FILE/LA0C03362_SI_001.PDF.
- Liu, Z., Wang, G., Xu, T., Deng, N., Xie, H., Zhang, X., 2024. Visible-light-driven peroxydisulfate activation by biochar-loaded Fe-Cu layered double hydroxide for penicillin G degradation: performance, mechanism and application potential. *Environ. Res.* 263, 120043. <https://doi.org/10.1016/J.ENVRRES.2024.120043>.
- Luo, Y., Zheng, A., Li, J., Han, Y., Xue, M., Zhang, L., Yin, Z., Xie, C., Chen, Z., Ji, L., Hong, Z., Xie, X., 2023. Integrated adsorption and photodegradation of tetracycline by bismuth oxycarbonate/biochar nanocomposites. *Chem. Eng. J.* 457, 141228. <https://doi.org/10.1016/J.CEJ.2022.141228>.
- Majhi, D., Das, K., Mishra, A., Dhiman, R., Mishra, B.G., 2020. One pot synthesis of CdS/BiOBr/Bi₂O₂CO₃: a novel ternary double Z-scheme heterostructure photocatalyst for efficient degradation of atrazine. *Appl. Catal. B Environ.* 260, 118222. <https://doi.org/10.1016/J.APCATB.2019.118222>.
- Moles, S., Ormad, M.P., Gomez, J., Szpunar, J., Bolea, E., Mosteo, R., 2024. Pilot plant approach combining photocatalysis and adsorption for antibiotics removal from slaughterhouse and urban wastewater treatment plant effluents. *Environ. Technol. Innov.* 34, 103586. <https://doi.org/10.1016/J.ETI.2024.103586>.
- Othmani, A., John, J., Rajendran, H., Mansouri, A., Sillanpää, M., Velayudhaperumal Chellam, P., 2021. Biochar and activated carbon derivatives of lignocellulosic fibers towards adsorptive removal of pollutants from aqueous systems: critical study and future insight. *Sep. Purif. Technol.* 274, 119062. <https://doi.org/10.1016/J.SEPUR.2021.119062>.
- Priya, A.K., Gnanasekaran, L., Rajendran, S., Qin, J., Vasseghian, Y., 2022. Occurrences and removal of pharmaceutical and personal care products from aquatic systems using advanced treatment- A review. *Environ. Res.* 204, 112298. <https://doi.org/10.1016/J.ENVRRES.2021.112298>.
- Recepoglu, Y.K., Goren, A.Y., Vatanpour, V., Yoon, Y., Khataee, A., 2022. Boron carbon nitride nanosheets in water and wastewater treatment: a critical review. *Desalination* 533, 115782. <https://doi.org/10.1016/J.DESAL.2022.115782>.
- Sasikumar, S., Rajaram, A., 2024. Unveiling the cobalt vanadate supported hexagonal boron nitride nanocomposite for photocatalytic wastewater treatment: enhanced degradation of dyes, antibiotics, and real industrial wastewater. *Mater. Sci. Semicond. Process.* 177, 108407. <https://doi.org/10.1016/J.MSSP.2024.108407>.
- Shahabuddin, S., Khanam, R., Khalid, M., Sarih, N.M., Ching, J.J., Mohamad, S., Saidur, R., 2018. Synthesis of 2D boron nitride doped polyaniline hybrid nanocomposites for photocatalytic degradation of carcinogenic dyes from aqueous solution. *Arab. J. Chem.* 11, 1000–1016. <https://doi.org/10.1016/J.ARABJC.2018.05.004>.
- Shamai Yamin, T., Shifrovitch, A., Madmon, M., Prihed, H., Weissberg, A., 2024. Structural elucidation of tramadol, its derivatives, and metabolites using chemical derivatization and liquid chromatography-high-resolution tandem mass spectrometry. *Rapid Commun. Mass Spectrom.* 38. <https://doi.org/10.1002/rcm.9881>.
- Shankar, R., Sachs, M., Francàs, L., Lubert-Perquel, D., Kerherve, G., Regoutz, A., Petit, C., 2019. Porous boron nitride for combined CO₂ capture and photoreduction. *J. Mater. Chem. A* 7, 23931–23940. <https://doi.org/10.1039/C9TA02793A>.
- Sun, Y., Shi, Q., Gu, X., Wang, B., Lumbers, B., Li, G., 2024. Exquisitely designed TiO₂ quantum dot/Bi₂O₂CO₃ nano-sheet S-scheme heterojunction towards boosted photo-catalytic removal. *J. Colloid Interface Sci.* 662, 76–86. <https://doi.org/10.1016/J.JCIS.2024.02.004>.
- Susanti, B., Warmadewanthi, I.D.A.A., Tangahu, B.V., 2022. Characterization and experimental evaluation of cow dung biochar + dolomite for heavy metal immobilization in solid waste from silica sand purification. *Bioresour. Technol.* Rep. 18, 101102. <https://doi.org/10.1016/J.BITEB.2022.101102>.
- Sutar, S., Otari, S., Jadhav, J., 2022. Biochar based photocatalyst for degradation of organic aqueous waste: a review. *Chemosphere* 287, 132200.
- Tambe, V.S., Deodhar, M.N., Prakya, V., 2016. LC and LC-MS study for simultaneous determination of tramadol hydrochloride and ketorolac tromethamine in bulk and formulation with their major degradation products. *Bull. Fac. Pharm. Cairo Univ.* 54, 87–97. <https://doi.org/10.1016/J.BFOPCU.2016.02.002>.
- Tan, Y., Zhou, Q., Huang, W., Lu, K., Yang, K., Chen, X., Li, D., Dionysiou, D.D., 2023. Highly efficient photocatalytic degradation over rose-like 1D/2D La(OH)₃(Bio)2 OHCl heterostructures boosted by rich oxygen vacancies and enhanced interfacial charge transfer. *Environ. Sci. Nano* 10, 215–228. <https://doi.org/10.1039/D2EN00792D>.
- Tie, W., Bhattacharyya, S.S., Ma, T., Yuan, S., Chen, M., He, W., Lee, S.H., 2025. Improving photoexisted carrier separation through Z-scheme W18O49/BiOBr heterostructure coupling carbon quantum dots for efficient photoelectric response and tetracycline photodegradation. *Carbon N. Y.* 231, 119707. <https://doi.org/10.1016/J.CARBON.2024.119707>.
- Veettil Vineesh, T., Vijayakumar Anagha, U., Purayil Dileep, N., Cheraparambil, H., Nambeesan, J., Shajumon, M.M., 2020. Enhanced bifunctional catalytic activity of cobalt phosphide flowers anchored N-doped reduced graphene oxide for hydrogen and oxygen evolution. *Chemelectrochem* 7, 3319–3323. <https://doi.org/10.1002/CELC.202000680>.
- Verbeken, M., Suleman, S., Baert, B., Vangheluwe, E., Van Dorpe, S., Burvenich, C., Duchateau, L., Jansen, F.H., De Spiegeleer, B., 2011. Stability-indicating HPLC-DAD/UV-ESI/MS impurity profiling of the anti-malarial drug lumefantrine. *Malar. J.* 10. <https://doi.org/10.1186/1475-2875-10-51>.
- Wang, A., Zhang, J., Zhao, W., Zhu, W., Zhong, Q., 2018a. Porphyrin decorated Bi₂O₂CO₃ nanocomposites with efficient disfunctional properties of photocatalysis and optical nonlinearity. *J. Alloys Compd.* 748, 929–937. <https://doi.org/10.1016/J.JALLCOM.2018.03.217>.
- Wang, P., Zhan, S., Wang, H., Xia, Y., Hou, Q., Zhou, Q., Li, Y., Kumar, R.R., 2018b. Cobalt phosphide nanowires as efficient co-catalyst for photocatalytic hydrogen evolution over Zn0.5Cd0.5S. *Appl. Catal. B Environ.* 230, 210–219. <https://doi.org/10.1016/J.APCATB.2018.02.043>.
- Wang, Z., Chen, M., Huang, Y., Shi, X., Zhang, Y., Huang, T., Cao, J., Ho, W., Lee, S.C., 2018c. Self-assembly synthesis of boron-doped graphitic carbon nitride hollow tubes for enhanced photocatalytic NO_x removal under visible light. *Appl. Catal. B Environ.* 239, 352–361. <https://doi.org/10.1016/J.APCATB.2018.08.030>.
- Wang, Q., Li, P., Zhang, Z., Jiang, C., Zuojiao, K., Liu, J., Wang, Y., 2019. Kinetics and mechanism insights into the photodegradation of tetracycline hydrochloride and ofloxacin mixed antibiotics with the flower-like BiOCl/TiO₂ heterojunction. *J. Photochem. Photobiol. Chem.* 378, 114–124. <https://doi.org/10.1016/J.JPHOTOCHEM.2019.04.028>.
- Wang, Y., Lei, Y., Liu, X., Song, L., Hamid, N., Zhang, R., 2022. Sulfonamide and tetracycline in landfill leachates from seven municipal solid waste (MSW) landfills: seasonal variation and risk assessment. *Sci. Total Environ.* 825, 153936. <https://doi.org/10.1016/J.SCITOTENV.2022.153936>.
- Wu, F., Zhou, C., Tang, Y., Han, J., Xing, W., Wu, G., Huang, Y., 2025. Engineering nickel doped cobalt phosphide as a photocatalyst toward visible-light-driven CO₂ reduction. *Mol. Catal.* 576, 114940. <https://doi.org/10.1016/J.MCAT.2025.114940>.
- Yazdi, S., Rezayat, M., Rovira, M., Electrocatalytic, J.J.R., Yazdi, M.S., Rezayat, M., Josep, J., Rovira, R., 2022. Electrocatalytic activity of nickel foam with Co, Mo, and Ni phosphide nanostuctures. *Plasma* 5, 221–232. <https://doi.org/10.3390/PLASMA5020017>, 221–232.
- Yu, H., Wang, D., Zhao, B., Lu, Y., Wang, X., Zhu, S., Qin, W., Huo, M., 2020. Enhanced photocatalytic degradation of tetracycline under visible light by using a ternary photocatalyst of Ag₃PO₄/AgBr/g-C₃N₄ with dual Z-scheme heterojunction. *Sep. Purif. Technol.* 237, 116365. <https://doi.org/10.1016/J.SEPPUR.2019.116365>.
- Zhang, X., Fan, X., Wang, X., Deng, T., Liu, E., Chen, B., 2020. Facile fabrication of Co₂P/TiO₂ nanotube arrays photoelectrode for efficient methylene blue degradation. *Colloids Surfaces A Physicochem. Eng. Asp.* 599, 124875. <https://doi.org/10.1016/J.COLSURFA.2020.124875>.
- Zhang, X., Cai, T., Zhang, S., Hou, J., Cheng, L., Chen, W., Zhang, Q., 2024. Contamination distribution and non-biological removal pathways of typical tetracycline antibiotics in the environment: a review. *J. Hazard. Mater.* 463, 132862. <https://doi.org/10.1016/J.JHAZMAT.2023.132862>.
- Zhao, H., Li, G., Tian, F., Jia, Q., Liu, Y., Chen, R., 2019. g-C₃N₄ surface-decorated Bi₂O₂CO₃ for improved photocatalytic performance: theoretical calculation and photodegradation of antibiotics in actual water matrix. *Chem. Eng. J.* 366, 468–479. <https://doi.org/10.1016/J.CEJ.2019.02.088>.
- Zhen, L., Xu, Y., Liu, J., Wu, Z., Shi, J., Deng, H., 2024. A novel 0D/2D Z-scheme heterojunction Bi₂Sn₂O₇/Bi₄O₇ for boosting tetracycline photodegradation: insight from performance to mechanism. *J. Water Process Eng.* 68, 106518. <https://doi.org/10.1016/J.JWPE.2024.106518>.
- Zhu, R., Yu, X., Li, W., Li, M., Bo, X., Gan, G., 2023. Cobalt nanoparticles-embedded porous carbon nanocages uniformly dispersed hollow carbon fibers as the accelerated electrocatalysts toward water splitting. *J. Alloys Compd.* 947, 169488. <https://doi.org/10.1016/J.JALLCOM.2023.169488>.